Die approbierte Originalversion dieser Diplom-/Masterarbeit ist an der Hauptbibliothek der Technischen Universität Wien aufgestellt (http://www.ub.tuwien.ac.at).

The approved original version of this diploma or master thesis is available at the main library of the Vienna University of Technology (http://www.ub.tuwien.ac.at/englweb/).

TECHNISCHE
UNIVERSITÄT
WIEN

VIENNA
UNIVERSITY OF
TECHNOLOGY

DIPLOMARBEIT

Optical Spectroscopy and Vertical Field Stark Shift of Single Self-Assembled InAs/GaAs Quantum Dots

eingereicht von

RADHA GOVINDA MADHAVA LILLEY

zum Zwecke

der Erlangung des akademischen Grades eines Diplomingenieurs

am

Institut für Photonik

der Technischen Universität Wien

unter der Anleitung von

Ass. Dipl.-Ing. Dr.techn. Wolfgang Parz

und

Univ.Prof. Mag.rer.nat. Dr.rer.nat. Karl Unterrainer

Wien, am 18. Dezember 2009

Zusammenfassung

Quantenpunkte sind Nanokristalle, deren Größe vergleichbar mit der de Broglie Wellenlänge langsamer Elektronen ist. Die Nanokristalle sind in einen Wirtskristall eingebettet und haben eine kleinere Bandlücke. Das Resultat dieser Struktur ist eine starke räumliche Einschränkung der Elektron- und Lochbewegung, die zur Quantisierung der Zustände und damit zu diskretisierten Energieniveaus ähnlich den Energieniveaus einzelner Atome führt. Daher werden Quantenpunkte auch künstliche Atome genannt. Das Ziel dieser Arbeit ist die Spektroskopie einzelner Quantenpunkte unter dem Einfluss eines der Wachstumsrichtung parallel gerichteten elektrischen Feldes bei verschieden starker optischer Anregung. Wird dem Quantenpunkt ein elektrisches Feld eingeprägt, so wird die Bandstruktur verkippt und die Energieniveaus erfahren eine Rotverschiebung. Dieser Effekt wird als Stark-Effekt bezeichnet.

Im Laufe dieser Arbeit wurden spektroskopische Methoden untersucht, die der Charakterisierung einzelner Quantenpunkte dienen können. Weiters werden Methoden, die den Zugriff auf einzelne Quantenpunkte erlauben, erörtert. Insbesondere sind Mikro-Photolumineszenzspektroskopie, Photostromspektroskopie und Starkverschiebungsgestützte Transmissionsspektroskopie von Interesse. Zum Zweck der Transmissionsspektroskopie wurde eine Probe mit Elektroden versehen, wobei die obere mit kleinen Aperturen versehen wurde. Weiters wurde ein Probenhalter für die Transmissionsspektroskopie entwickelt, der eine optische und elektronische Abschirmung des Photodetektors erlaubt.

In dieser Arbeit wird gezeigt, dass die Lumineszenz des GaAs-Wirtskristalls innerhalb der Bandlücke auf die Silizium-Dotierung zurückzuführen ist. Weiters wird die Ausprägung angeregter Zustände bei steigender Anregungsleistung gezeigt. Abschließend wird die Starkverschiebung einzelner InAs/GaAs-Quantenpunkte für ansteigende vertikal eingeprägte elektrische Felder und für verschiedene Anregungsleistungen präsentiert.

Die Analyse der Starkverschiebungsdaten hat das Vorhandensein eines permanenten Dipolmomentes in InAs-Quantenpunkten gezeigt, das von Quantenpunkt zu Quantenpunkt unterschiedlich stark ausgeprägt sein kann. Aus den Starkverschiebungsdaten wurden auch das Dipolmoment und die Polarisierbarkeit der Quantenpunkte ermittelt. Aus dem Dipolmoment wurde die Dipollänge berechnet und aus der Polarisierbarkeit wurde geschlossen, dass die Quantenpunkte ähnlich groß und ähnlich zusammengesetzt sein müssen.

Abstract

Quantum Dots are nanocrystals that are comparable in size to the de Broglie wavelength of slow electrons and are embedded in a host matrix with a larger band gap. As a result, the motion of electrons and holes is strongly confined within the nanocrystal, which gives rise to discrete energy levels similar to those observed for individual atoms. This is why they are also referred to as artificial atoms. In this work, the spectroscopy of single self-assembled Quantum Dots under the influence of an electric field parallel to the growth direction and under varying excitation intensities is carried out. By applying an electric field to the dots, the energy levels can be shifted, which is known as the Stark shift, and the measurement of this effect for a field in growth direction will be the main focus of this thesis.

During the course of this work, several spectroscopic techniques were investigated, including conventional micro photoluminescence spectroscopy, photocurrent spectroscopy and Stark shift assisted transmission spectroscopy. For the purpose of performing Stark shift assisted transmission spectroscopy a sample with a contacted bottom Si:GaAs layer and an Au electrode with several apertures for single dot access was fabricated. Additionally, a novel sample holder which provides electrical and stray light shielding for the optical detector beneath the sample was developed.

Measurement results presented here, include sub-band-gap luminescence of the GaAs bulk due to Si doping, evolution of excited quantum dot states under variable excitation power and the vertical field Stark shift of single self-assembled InAS Quantum Dots in a GaAs host matrix.

The analysis of the Stark shift data shows the existence of permanent dipole moments that vary from dot to dot. By fitting the Stark shifts, the built-in dipole moment and the polarizability of the dots was determined. From the dipole moment, the dipole length was derived, and from the polarizabilities, which were quite similar for the analyzed dots, it was concluded that the dots were comparable in size and composition.

Contents

Contents **vii**

1 Introduction **1**

1.1 An introduction to Quantum Dots . . . 1

1.2 Fabrication of Quantum Dots . . . 3

1.2.1 Lithographic and pre-patterning fabrication techniques . . . 3

1.2.2 Self-organized fabrication techniques . . . 5

1.3 Quantum Dot Applications . . . 7

1.3.1 Sensors . . . 7

1.3.2 Emitters . . . 10

1.3.3 Computing . . . 11

2 Theoretical Background **13**

2.1 Electronic states in Quantum Dots . . . 13

2.2 Coulomb interactions . . . 16

2.3 Carrier relaxation mechanisms . . . 18

2.4 Electronic control of Quantum Dot states . . . 21

3 Experimental Methods **25**

3.1 Sample structure and processing . . . 25

3.2 Photoluminescence spectroscopy . . . 29

3.3 Photocurrent spectroscopy . . . 33

3.4 Transmission spectroscopy . . . 34

4 Measurements and Discussion **41**

4.1 μPL measurements . . . 41

4.1.1 Quasi-ensemble aperture 41
4.1.2 Single dot aperture 42
4.1.3 Single dots under varying excitation intensity 44
4.1.4 Discussion 45
4.2 Stark Shift measurements 47
4.2.1 Stark shift under high excitation power 49
4.2.2 Stark shift under low excitation power 51
4.2.3 Discussion 51

Conclusions **57**

Acknowledgements **59**

Recipes **61**

Bibliography **64**

Chapter 1

Introduction

Towards the end of the 1970s and the beginning of the 1980s research of confined systems had mainly focused on 2D structures such as quantum wells and super lattices, which were by then fairly well understood. In the early 80s, research interest began to shift to 1D and 0D structures (Bimberg et al., 1999) since confinement in all three dimensions was expected to yield discrete electronic states which can be engineered by merely adjusting the size of the structure. The ability to engineer electronic states makes 0D structures or so-called Quantum Dots (QD) very interesting for many photonic, telecommunication and sensor applications. QDs are also used as model systems to investigate fundamental physics and have been proposed for quantum computing applications (Biolatti et al., 2000).

1.1 An introduction to Quantum Dots

QDs are particles comparable in size to the de Broglie wavelength of slow electrons

$$\lambda = \frac{h}{p} = \frac{h}{m^* v_{th,3D}} = \frac{h}{\sqrt{3m^* k_B T}} \tag{1.1}$$

where h is Planck's constant, m^* is the effective electron mass, $v_{th,3D}$ the thermal velocity for a particle with three degrees of translational freedom, k_B is the Boltzmann constant and T is the temperature. Assuming the effective electron mass $m^* = 0.063 m_e$ of GaAs in the Γ-valley, the de Broglie wavelength at 300 K is 24.8 nm, thus giving a rough estimate of the size of a GaAs QD. In this domain quantization effects on the motion of charge carriers become significant. Consider the simple example of the infinitely deep potential box measuring $L_xL_yL_z$ with the discrete energy levels

$$E_n = \frac{\hbar^2 k^2}{2m^*} \tag{1.2}$$

where $\hbar$ is the reduced Planck's constant, $k^2 = k_x^2 + k_y^2 + k_z^2$, $k_i = \frac{n_i \pi}{L_i}$ and $n_i \in \mathbb{N}$. Now the transition energy from the ground state to the first excited state for a particle $i \in \{e, h\}$ can be calculated as follows

$$\Delta E_{i,1\rightarrow 2} = E_2 - E_1 = \frac{\hbar^2 k_2^2}{2m_i^*} - \frac{\hbar^2 k_1^2}{2m_i^*} = \frac{\hbar^2}{2m_i^*}\left(k_{z,2}^2 - k_{z,1}^2\right) = \frac{3\hbar^2\pi^2}{2L^2 m_i^*}. \tag{1.3}$$

Remember that for equation 1.3 the excited state was chosen in the z direction and therefore $k_{x,1} = k_{x,2} = \pi/L_x$, $k_{y,1} = k_{y,2} = \pi/L_y$, $k_{z,1} = \pi/L_z$ and $k_{z,2} = 2\pi/L_z$ are the set of k values for the ground and excited state. Now, while remembering that for interband QDs both electrons and holes are confined, one finds that the difference in transition energy from the ground state to the first excited state is given by

$$\Delta E = \Delta E_{e,1\rightarrow 2} + \Delta E_{h,1\rightarrow 2} = \frac{3\hbar^2\pi^2}{2L_z^2}\left(\frac{1}{m_e^*} + \frac{1}{m_h^*}\right) \tag{1.4}$$

which for a GaAs cube of the size $L_x = L_y = L_z = 24.8$ nm (the de Broglie wavelength) equates to 32.7 meV and is comparable to k_BT at room temperature. In a more realistic scenario, the potential well would be finitely deep and the wave functions would penetrate into the barriers thus lowering ΔE. This roughly shows that the maximum size of a QD has an upper bound which is determined by the operating temperature. If either the dot size becomes greater or the operating temperature is increased, the thermal energy of the electrons will mask the discrete energy levels and quantization effects disappear.

Additionally, due to the finite barrier height of the potential well a minimum size for QDs exists, where the ground state is too high to be contained. The minimum dot size is given by

$$L_{min} = \frac{\pi\hbar}{\sqrt{2m_e^*\Delta E_c}} \tag{1.5}$$

where ΔE_c is the difference in conduction band energy of the substrate and dot material (Bimberg et al., 1999).

Revisiting equation 1.2, one also finds that the energy levels inversely depend on L^2 of the potential well. Therefore, by manipulating merely the size of the dot, the energy levels can be controlled, which to a degree relieves the restrictions encountered in bulk material systems, such as specific gap energy, unavailable gap energies in the far infrared and THz range and impossible luminescence in indirect gap materials like Si. The relief of the last case for instance, has been demonstrated by Pavesi et al. (2000) as they have achieved luminescence and optical gain with Si.

However, this picture is still very simplistic. QDs do not come in cubic or perfect spherical form, equal size and arbitrary barrier height and there are limits to the achievable wavelength range as well. These shortcomings and limitations are partly due to the used material system and the way QDs are fabricated.

1.2 Fabrication of Quantum Dots

Three-dimensional confinement inexorably leads to the initial, somewhat naive, notion of a tiny box that can be fabricated with conventional epitaxial and lithographic techniques. One, however, finds that the dots created by such techniques are not suitable for optical applications and thus further research led to pre-patterning and self-organized QD fabrication. Lithographic and pre-patterning fabrication will be discussed in section 1.2.1, followed by a discussion of self-organized fabrication and the effects of capping in section 1.2.2.

1.2.1 Lithographic and pre-patterning fabrication techniques

Early attempts at creating QDs were straightforward and used lithographic techniques to etch quantum wells into shape, thus allowing for accurate control over dot size, shape and position. The etching process, however, introduces impurities and heavily damages the dot surface, which increases the non-radiative recombination rate and is generally not desirable for optical devices. An improvement over this technique was growing QDs on patterned substrates. Here inverse pyramids are etched into the substrate, followed by the deposition of the dot material, which creates well-defined QDs at the bottom. Alternatively, truncated pyramid structures can be used to grow QDs on the flat top. The most important condition that needs to be fulfilled for this fabrication technique to work is that the growth rate of the QD crystal material is higher on the flat top of the truncated pyramid than on the side walls (Masumoto and Takagahara, 2002; Bimberg et al., 1999). While these approaches represent some degree of self-organized QD growth, they still require a considerable amount of processing and structuring of the substrate

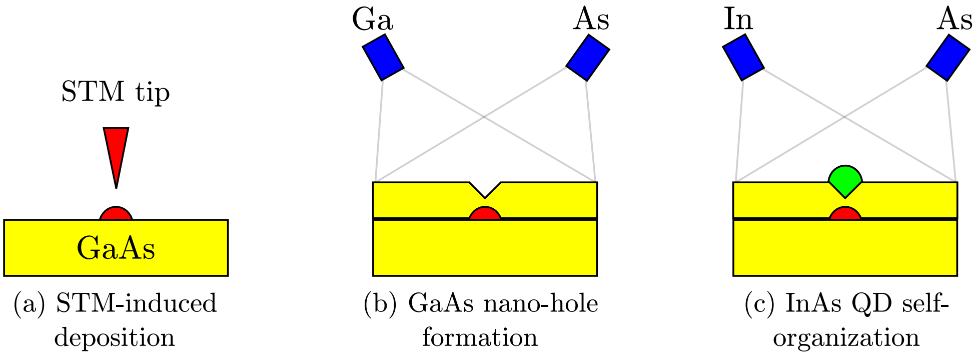

(a) STM-induced deposition

(b) GaAs nano-hole formation

(c) InAs QD self-organization

Figure 1.1: Fabrication prcedure for InAs SCQDs on GaAs reproduced from Kohmoto et al. (1999).

and only yield low dot densities. However, the dot densities produced by lithographic techniques are still mainly limited by the lithographically achievable structure sizes, as an interesting approach by Kohmoto et al. (1999) that uses scanning tunneling microscope (STM) nano lithography combined with self-organizing growth to create site controlled QDs (SCQDs) illustrates. STM assisted nano lithography is achieved by positioning a tungsten STM tip over the desired QD growth site upon a GaAs sample and then applying five 7 V/10 nA/500 ms pulses in 10 ms intervals, thus creating a nano-deposit. The nano-deposit then acts as a mask. Thereafter a thin layer of GaAs is grown on top of the sample via MBE. As GaAs can not grow directly over the tungsten deposition sites, nano holes are formed above the nano-deposits. Now 1.1 ML InAs is deposited on the sample that fills the holes and planarises the sample, leaving – as the authors assume but did not verify – In(Ga)As inside the hole. Since In(Ga)As has a lattice constant comparable to InAs, QDs will preferably grow mostly above the nano-deposits. This process is illustrated in figure 1.1 and the resulting STM image of the SCQDs is shown in figure 1.2. Kohmoto et al. (1999) reported dots with a base diameter of 35 nm, a height of 6 nm and a 45 nm pitch, and essentially achieve dot densities comparable to fully self-organized fabrication techniques with densities ranging from 10^9 cm^{-2} to 10^{10} cm^{-2} (Chen et al., 2001; Garcia et al., 1997; Saito et al., 1998; Le Ru et al., 2003).

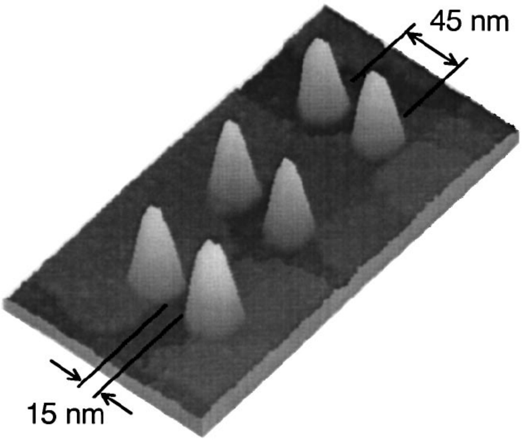

Figure 1.2: STM image of three InAs SCQD pairs. The QDs all have a 30 nm base diameter and are 6 nm high. The image was reproduced from Kohmoto et al. (1999).

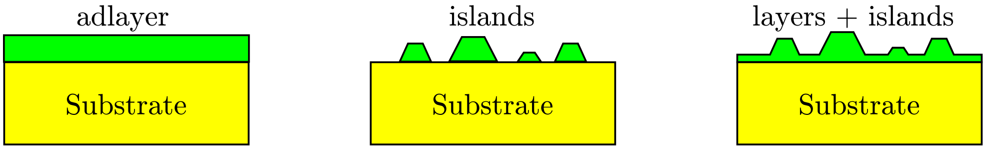

(a) Frank-van der Merwe growth (b) Volmer-Weber growth (c) Stranski-Krastanov growth

Figure 1.3: Schematic of the Frank-van der Merwe (a), Volmer-Weber (b) and Stranski-Krastanov (c) growth modes.

1.2.2 Self-organized fabrication techniques

The techniques mentioned above that feature self-assembly all require considerable processing effort prior to QD growth, ultimately resulting in longer manufacturing time, more expensive devices and – in some cases – dots with low optical quality. It was discovered by Stranski and Krastanov that crystals grown on a substrate with mismatching lattice constants first grow in a strained layer-by-layer (or Frank-van der Merwe, FM) growth mode and, after some amount of deposited layers, in an island (or Volmer-Weber, VW) growth mode. This combined growth mode is known as the Stranski-Krastanov (SK) growth and is detailed along with the FM and VW growth modes in figure 1.3.

Essentially, these growth modes can be characterized as follows

$$\epsilon_2 + \gamma_{1,2} > \epsilon_1 \Rightarrow \text{Frank-van der Merwe growth} \tag{1.6}$$

$$\epsilon_2 + \gamma_{1,2} < \epsilon_1 \Rightarrow \begin{cases} \text{Volmer-Weber growth} & \text{for unstrained adlayer,} \\ \text{Stranski-Krastanov} & \text{for strained adlayer.} \end{cases} \tag{1.7}$$

with the substrate surface energy ϵ_1, the adlayer surface energy ϵ_2 and the interface energy $\gamma_{1,2}$. Hence island formation is the result of strain energy minimization and SK growth only occurs in strained systems (Eaglesham and Cerullo, 1990; Bimberg et al., 1999).

Closely observing the crystal growth mechanisms, one finds that the mode in which deposited material tends to grow also depends on the processing parameters. Firstly, high deposition rates lead to a preferred layer-by-layer growth because less time is available for nucleation of islands. Secondly, higher substrate temperatures promote island growth due to the weaker bond of the substrate with the adatoms. Thirdly, if the adatom-to-adatom bonding is stronger than the substrate to adatom bonding, again island growth is favored. Finally, as mentioned before, the lattice mismatch

$$\sigma = \frac{\alpha - \beta}{\beta} \tag{1.8}$$

plays a major role in growth mode selection (α is the lattice constant of the adlayer and β is the lattice constant of the substrate). For negligible mismatch, strain is negligible and if $\epsilon_2 + \gamma_{1,2} > \epsilon_1$ holds, layer-by-layer growth is preferred, thus enabling conventional epitaxy. For moderate mismatch with $\epsilon_2 + \gamma_{1,2} < \epsilon_1$ and slow deposition of adatoms, SK or even VW growth is possible. It is common to introduce the critical mismatch at this point, as it is used as the boundary where the FM growth mode can evolve into the SK or VW growth mode. For instance, above the critical mismatch of 1.8%, SK growth occurs for $\mathrm{In}_x\mathrm{Ga}_{1-x}\mathrm{As}$ ($x \geq 0.25$) and below the critical mismatch layer-by-layer growth is accommodated by dislocations (Markov, 1995; Seifert et al., 1997). For higher deposition rates the critical mismatch increases as well, since less time for island nucleation is available and layer-by-layer growth with dislocations occurs instead. Another parameter relevant to growing QDs is the critical thickness, which is related to SK growth and describes the point where islands begin to form during the deposition of material. For InAs on GaAs a critical thickness of 1.5 ML (monolayers) for a substrate deposition temperature of 530 °C was determined (Leonard et al., 1994). It is also worth mentioning that the critical mismatch is somewhat arbitrary since lower deposition rates combined with lower mismatch values have been shown to also achieve SK growth with a much larger critical thickness (Eaglesham and Cerullo, 1990).

To complete the fabrication process, the QD layer must be capped. Capping the QDs serves the purpose of protecting the QDs, providing a flat surface for further processing and controlling the potential depth of the dot. Capping, however, also introduces additional strain and alters the shape of the QD, thus altering the wave functions and energy levels. It has been shown that a 100 nm GaAs capping layer over InGaAs QDs on a GaAs substrate increases the emission energy by 287 meV at room temperature (Saito et al., 1998).

1.3 Quantum Dot Applications

In bulk semiconductor systems the emission and absorption energy depends heavily on the selected material system. This becomes a burden when the required absorption or emission energy determines a material system that is difficult to process and consequently can make an application unfeasible. Thus, QDs and their potentially material-independent absorption and emission spectrum were seen as the solution for the limitations of bulk material systems. This led to the development of several applications in the fields of opto-electronics and computing. Recent progress and improvements that have been made by the use of QDs in sensor applications will be discussed in 1.3.1 followed by light emitters in section 1.3.2 and computing in section 1.3.3.

1.3.1 Sensors

Infrared sensors and infrared image sensors are popular devices for many applications within the commercial, military and medical fields. However, the fabrication of conventional IR sensors based on exotic material systems and complex structures, such as micro bolometers, thermopiles or Golay cells, is costly. Self-organized QD based sensors were expected to be much cheaper since they can be fabricated from well-understood materials with existing technology. This led to the increasing popularity of research in the field of optical QD sensors. In order to evaluate the improvements over conventional systems and for further use later on, the figures of merit responsivity, noise equivalent power (NEP), noise equivalent temperature difference (NETD) and the normalized detectivity require at least a brief definition. The responsivity is defined as the output parameter in relation to the input radiation power. Depending on the sensor type, the output parameter is usually a voltage or current. Therefore, the responsivity is $R = U_{out}/P_{Ph}$ or $R = I_{out}/P_{Ph}$.

The noise equivalent power (NEP) is defined as the signal power that gives a signal to noise ratio of unity or, alternatively, as the ratio of the noise equivalent output parameter and the device responsivity

$$\mathrm{NEP} = U_n/R \text{ or} \tag{1.9}$$

$$\mathrm{NEP} = I_n/R \tag{1.10}$$

depending on the device type. Note that the noise can be thermal noise (Johnson noise), shot noise, generation/recombination noise or one-over-f noise, and depending on the device type one or several noise processes will limit device performance.

The noise equivalent temperature difference (NETD or NEΔT) is closely related to the NEP. The NETD is the temperature difference an object requires in order to yield the NEP above which it is distinguishable from the thermal background and therefore is more commonly used than the NEP.

The normalised detectivity D^* is the inverse normalized NEP. And since $\mathrm{NEP} \propto U_n$ (or $\mathrm{NEP} \propto I_n$), $U_n \propto \sqrt{P_n}$ (or $I_n \propto \sqrt{P_n}$) and $P_n \propto A\Delta f$ where A is the detector surface and Δf is the noise bandwidth, the NEP is normalized to $\sqrt{A\Delta f}$, in order to remove the device geometry and frequency characteristics from the figure of merit. This results in the normalized detectivity $D^* = \sqrt{A \cdot \Delta f}/\mathrm{NEP}$ (Kovacs, 1998; Wallrabe, 2001).

As for applications, a QD based broadband infrared imager that uses a multi-transition mechanism[1] has been demonstrated by Tang et al. (2006). They detected peak wavelengths of 4.1 μm to 9.5 μm at 140 K which can be tuned via a bias voltage (see Stiff et al. (2001)). Tang et al. (2006) also achieved a peak detectivity of $1.5 \cdot 10^{10}$ cm$\sqrt{\mathrm{Hz}}$/W at 80 K and 0.3 V bias with their 256 × 256 QDIP focal plane array. The noise current was $5.3 \cdot 10^{-13}$ A/$\sqrt{\mathrm{Hz}}$ and the pixel size was 100×100 μm^2 resulting in a responsivity of 795 mA/W. The authors also presented images taken at temperatures as high as 135 K, as can be seen in figure 1.4.

---

[1] By multi-transition mechanism, the excitation of carriers from discrete QD levels to the wetting layer is meant. See Huang et al. (2005) for details.

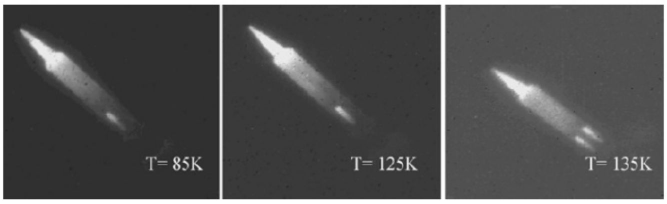

Figure 1.4: Thermal images of a soldering iron head at substrate temperatures of 85 K, 125 K, and 135 K, respectively with $T_{int} \approx 16$ ms reproduced from Tang et al. (2006).

Despite the advantages QDs provide, they also suffer a considerable drawback: a low dot density which results in low external quantum efficiency. To improve this, a hybrid dot-in-a-well structure is used and argued to have a higher quantum efficiency than conventional QDIPs but yields a lower photoconductive gain (Gunapala et al., 2007). The reported DWELL structure has a 200×200 μm^2 pixelsize and 25 μm pitch. The device achieves an NETD of 40 mK at 60 K and a detectivity of $\sim 1 \cdot 10^{10}$ cm$\sqrt{\text{Hz}}$/W at 77 K and 8.1 μm.

The close relationship sensors and energy converters share also leads to applications where QDs are embedded in solar cells or completely replace the conventional bulk material. An example are functionalized TiO_2 nanocrystallites bound to CdSe QDs that can be coated onto a transparent electrode as done by Robel et al. (2006), which is a potentially cost-effective way to fabricate solar cells.

Thus far, applications related to processes where one photon generates at most one exciton (electron-hole pair) have been discussed, since in bulk material systems it is most probable to generate an exciton and a phonon from a photon with $\hbar\omega \geq E_g$. However, carrier multiplication, which is the result of Impact Ionization – the inverse process to Auger Recombination – was already observed in the 1950s (Schaller and Klimov, 2004). This allows more than one exciton to be generated for every high energy photon, as illustrated in figure 1.5. This process can potentially increase the conversion efficiency of solar cells, improve performance of avalanche photodiodes or allow more effective population inversion in laser systems. However, Impact Ionization (II) and Auger Recombination (AR) are inefficient due to energy and momentum conservation restrictions in bulk materials and thus were rarely used. In QDs II and AR become efficient because the restrictions are alleviated due to enhanced Coulomb interactions and relaxed momentum conserva-

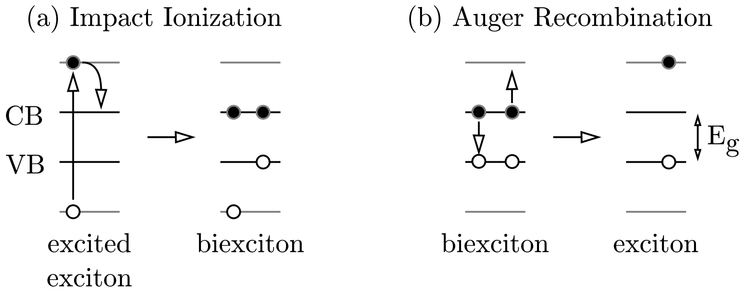

Figure 1.5: Illustration of the Impact Ionization (a) and Auger Recombination (b) processes reproduced from Schaller and Klimov (2004).

tion, since momentum is no longer a good quantum number (Schaller and Klimov, 2004; Ellingson et al., 2005). Also quantum yields of 218% (≥ 2 excitons per incident photon on average) were observed by Schaller and Klimov (2004) and quantum yields of 300% by Ellingson et al. (2005) in PbSe QDs, thus providing empirical evidence for efficient multi exciton generation in QDs. Schaller and Klimov (2004) also argued that conversion efficiencies of 60.3%, which is well above the theoretical limit of 43.9% for solar cells without MEG, are possible when the II threshold is optimized.

1.3.2 Emitters

Achieving cost-effective optical communication devices on the same chip as the processing electronics has long been challenging because Si is an indirect band gap material. This hindrance can be overcome by using Si QDs as light emitters. For instance, electroluminescence and tunability from 600 nm to 800 nm via bias voltage have been demonstrated at room temperature for Si QDs embedded in SiO_2 (Photopoulos and Nassiopoulou, 2000).

White light emitting diodes can also be realized with QDs as demonstrated by Damilano et al. (1999). Here, GaN QDs in AlN have been grown in different sizes by adjusting the adlayer thickness between 3 ML and 12 ML, thus allowing luminescence of orange to blue light. By stacking four layers of different QD sizes, white light emission was achieved.

A narrow line width and accurate control over the emission wavelength is important for telecommunication lasers that require a stable center frequency at 1.3 μm or 1.55 μm. However, QDs also offer additional advantages, such as long wavelength emission, lower threshold current, lower threshold temperature sensitivity, and higher differential gain

(Huffaker and Deppe, 1998). QD lasers have been shown to have threshold current densities of 16-26 A/cm^2 (Liu et al., 2000), which is well below reported quantum well laser threshold currents of 84 A/cm^2 (Hu et al., 1994) and 63 A/cm^2 (Salhi et al., 2004). Additionally, a linewidth enhancement factor of 0.1 has been measured for an InAs QD laser (Newell et al., 1999) as opposed to values of 1-2 which are considered to be very good for QW lasers (Bimberg et al., 1999). Low linewidth enhancement factors achieved by QD lasers allow for higher power outputs and less chirp, thus making QD lasers promising candidates for high power lasers and amplifiers as well as for telecommunication lasers that can be directly modulated as shown by Mi et al. (2005).

1.3.3 Computing

QDs are not limited to sensor/emitter applications or on-chip communication infrastructure. Applications for quantum computation with QDs (Loss and DiVincenzo, 1998) and a QD memory device (Bimberg et al., 1999) have been proposed, and state preparation, coherent manipulation and projective readout of double QDs made from electrostatic gates on a 2DEG have been demonstrated Petta et al. (2005). Also, as demonstrated by Li et al. (2003), a single self-assembled QD can be used to create a CROT gate. The used technique is not scalable though and limited to only two qubits.

Chapter 2

Theoretical Background

In the introductory chapter, a rough outline of QD properties was presented, followed by a coarse overview of fabrication techniques and applications. In this chapter, the picture presented thus far will be refined and the theory relevant to this thesis will be discussed in more detail. At first a more accurate model of QDs will be constructed in section 2.1, followed by the addition of Coulomb interactions in section 2.2 which can be the source of considerable discrepancy in measured and expected energy levels when not considered. Thereafter, carrier relaxation mechanisms within QDs will be the focus of section 2.3, and electrical manipulation of QD states in section 2.4 will finalize this chapter.

2.1 Electronic states in Quantum Dots

The model discussed in section 1.1 was sufficient to illustrate the discrete energy levels and size limitations of QDs. However, it assumed a simple cubic geometry and infinite potential barriers while neglecting carrier-carrier interactions and external fields. For QDs, a geometry that is closer to reality is a flat cylinder or lens shape. This shape is then approximated by a well-type confining potential in growth or z-direction and a 2D harmonic oscillator in the radial direction or xy-plane. Since the 2D harmonic oscillator is a special case of the 2D parabolic potential barrier (2D PPB) problem, one can use the Hamiltonian

$$H = -\frac{\hbar^2}{2m^*}\nabla^2 - V_{xy} - V_z \tag{2.1}$$

and the potentials

$$V_{xy} = \frac{m\gamma^2}{2}\left(x^2 + y^2\right) \tag{2.2}$$

$$V_z = \begin{cases} 0 & 0 < z < h, \\ \infty & z < 0 \vee z > h \end{cases} \tag{2.3}$$

to find that the eigenvalues of the 2D PPB are the sum of two 1D PPB eigenvalues

$$E_{xy} = E_x + E_y \tag{2.4}$$

with

$$E^{\pm}_{x,y} = \mp i\left(n_{x,y} + \frac{1}{2}\right)\hbar\gamma, \text{ where } n_i \in \mathbb{N}. \tag{2.5}$$

Superposing the 1D PPB eigenvalues results in four 2D PPB types with two $(n_x + n_y + 1)$-fold degenerate and two infinitely degenerate types (Shimbori and Kobayashi, 2000). For this case only the $(n_x + n_y + 1)$-fold degenerate cases

$$E^{\pm\pm}_{xy} = E^{\pm}_x + E^{\pm}_y = \mp i\left(n_x + n_y + 1\right)\hbar\gamma \tag{2.6}$$

are of interest as they represent the 2D harmonic oscillator. Thus the resulting energy levels (eigenvalues) of the lens-shaped dot can be composed of a superposition of the 2D PPB and infinite barrier well eigenvalues as follows:

$$E_{lmn} = E_l + E_{mn} = E_l + |E_{xy}| = \frac{\pi^2\left(l+1\right)^2\hbar^2}{2m^*h^2} + \left(m+n+1\right)\hbar\gamma. \tag{2.7}$$

Note that h is the height of the dot, γ is the harmonic oscillator frequency and that $n_x = m$, $n_y = n$ and $n_z = l$. Examining equation 2.7, one finds that for a fixed l, the energy levels are quantisized in units of $\hbar\gamma$ under the condition $m + n = \text{const}$. Assuming $l = 0$ and $m + n = 1$ one finds a two-fold degeneracy, namely the same E_{lmn} for the cases $|m = 1, n = 0\rangle = |10\rangle$ and $|m = 0, n = 1\rangle = |01\rangle$ thus allowing for four distinct particle states or a four-fold degeneracy when electron spin degeneracy $\pm\frac{1}{2}$ is considered. For $m + n = 2$ one finds a six-fold degeneracy $|02\rangle$, $|20\rangle$ and $|11\rangle$ and for $m + n = 3$ one finds an eight-fold degeneracy and so forth yielding a $2\left(n + m + 1\right)$ degeneracy with $\pm\frac{1}{2}$ spin. Drawing an analogy to the nuclear structure, $m + n = 0, 1, 2, ...$ are labeled s-, p-, d-, ... shells. If optical transitions are of interest, two further selection rules need to be introduced. Firstly $\Delta S = 0$ has to hold for spin, and secondly the total angular

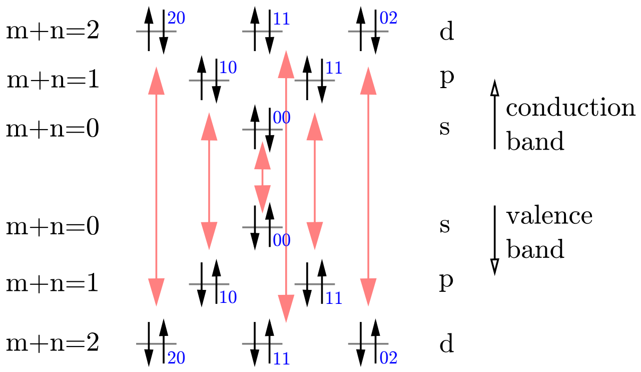

Figure 2.1: Illustration of the atomic shells and allowed optical transitions for a 2D harmonic oscillator for electrons and holes.

momentum J must vanish (Fasching, 2006; Krall, 2008), otherwise an optical transition under ideal circumstances is impossible. The summation of the angular momentum for electrons $j_e = n_e - m_e$ and the angular momentum for holes $j_h = m_h - n_h$ (Hawrylak, 1999) results in the total angular momentum $J = j_e + j_h = (n_e - n_h) - (m_e - m_h)$. The only way $J = 0$ can be achieved is if $\Delta n = n_e - n_h = 0$ and $\Delta m = m_e - m_h = 0$.

Proof: We define $n_e + m_e$ as the integer α_e since it must be a constant and analogously for $n_h + m_h = \alpha_h$ with $\alpha_{e,h} \geq 0$. We further know that $(n_e - n_h) - (m_e - m_h) = 0$ must hold, which results in the set of equations

$$n_e + m_e = \alpha_e \tag{2.8}$$

$$n_h + m_h = \alpha_h \tag{2.9}$$

$$n_e - m_e = n_h - m_h. \tag{2.10}$$

Reformulating the equations 2.8 and 2.9 yields $n_{e,h} = \alpha_{e,h} - m_{e,h}$ and inserting this into equation 2.10 results in $\alpha_e - \alpha_h = \Delta\alpha = 2\Delta m$. Equation 2.10 also implies $\Delta n = \Delta m$ and thus implies $\Delta n = \Delta m = \Delta\alpha/2$ but the difference of equation 2.8 and 2.9 implies $\Delta\alpha = \Delta n - \Delta m$ and thus $\Delta\alpha = \Delta m = \Delta n = 0$ must hold. Or in summary, only s-s, p-p, d-d, ... transitions with opposing spins are allowed optical transitions. The progression of states for $l = 0$ along with allowed optical transitions is depicted for electrons and holes in figure 2.1. One should note though, that this is only valid for a perfectly lens-shaped QD. Should this not be the case, these selection rules have to be reformulated.

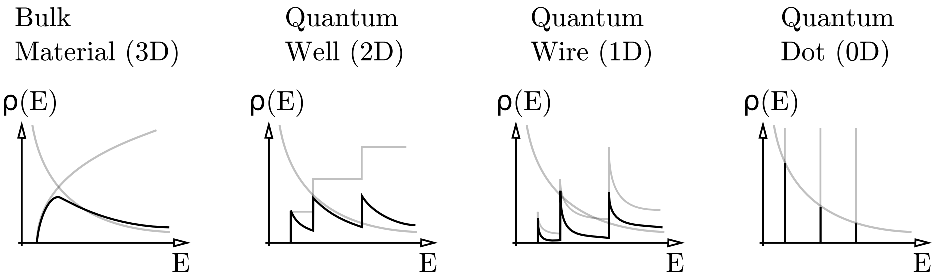

Figure 2.2: Illustration of the carrier density with the density of states and distribution function superimposed.

When discussing states of a system, one should also remember the connection between the density of states and the actual carrier density which is given by

$$\rho(E) = f(E) \cdot N(E) \tag{2.11}$$

with the state density $N(E)$ and the carrier distribution function $f(E)$. The proportionality of the density of states and confinement varying from 0 to 3 dimensions is given by

$$\begin{aligned} N_{3D}(E) &\propto \sqrt{E}, & (2.12)\\ N_{2D}(E) &\propto \sum_n \sigma(E - E_n), & (2.13)\\ N_{1D}(E) &\propto \sum_{n_x,n_y} \frac{\sigma(E - E_{n_x,n_y})}{\sqrt{E - E_{n_x,n_y}}}, & (2.14)\\ N_{0D}(E) &\propto \sum_n \delta(E - E_{n_x,n_y,n_z}) & (2.15) \end{aligned}$$

with the step function $\sigma(E)$ and the Dirac delta function $\delta(E)$. This is also illustrated in figure 2.2.

2.2 Coulomb interactions

Thus far, only single carrier confinement has been examined and interactions between carriers were not considered. Investigating the charge carrier confinement in QDs, one finds that both electrons and holes are captured and confined within the dot and are thus able to interact. Indeed, this can be expressed by a dipole or Coulomb potential

$$V_c = \frac{1}{4\pi\epsilon_0\epsilon_r}\frac{q_i q_j}{d_{ij}} \text{ with } d_{ij} = |\mathbf{r_i} - \mathbf{r_j}| \tag{2.16}$$

which is then added to the Hamiltonian in equation 2.1 thus resulting in

$$H = H_e + H_h + H_c = -\frac{\hbar^2}{2m_e^*}\nabla_e^2 - \frac{\hbar^2}{2m_h^*}\nabla_h^2 + V_e\left(\mathbf{r_e}\right) + V_h\left(\mathbf{r_h}\right) + V_c. \tag{2.17}$$

It is worth noting that for excitons the Coulomb potential causes an attraction and thus lowers the energy of the system while the electron-electron/hole-hole interaction is repulsive and increases the energy.

Depending on the size of the QD and the barrier height, three confinement regions for excitons can be distinguished in order to determine if the Coulomb interaction has a noticeable effect. Firstly if the QD diameter L is smaller than the excitonic Bohr radius a_B, the confining potential of the dot will be much larger than the Coulomb potential and thus the Coulomb potential can be neglected. This is the strong confinement regime and neglecting the Coulomb potential is justifiable. If the opposite is the case and $L > a_B$, then the Coulomb potential will be roughly comparable to the QD confining potential. This is the weak confinement regime and the Coulomb potential can not be neglected. Finally, confinement energy can also be comparable to Coulomb energy. Here the electron confinement is larger than the Coulomb energy and the hole confinement is smaller. Thus the hole energy quantization results from the electrostatic (Coulomb) potential. This can arise for QDs where the effective masses of electrons and holes are significantly different (Bimberg et al., 1999). This regime is the intermediate confinement regime.

The statement made with equation 2.17, however, is only valid for a single exciton, as multiple excitons within a dot must also include electron-electron, hole-hole and electron-hole interactions while accounting for exciton creation and annihilation, ultimately yielding the following Hamiltonian

$$\begin{aligned} H \quad &= \sum_i E_i^e c_i^\dagger c_i + \sum_i E_i^h h_i^\dagger h_i - \sum_{ijkl} \langle ij \left| V_{eh} \right| kl \rangle c_i^\dagger h_j^\dagger h_k c_l \\ &+ \tfrac{1}{2} \sum_{ijkl} \langle ij \left| V_{ee} \right| kl \rangle c_i^\dagger c_j^\dagger c_k c_l + \tfrac{1}{2} \sum_{ijkl} \langle ij \left| V_{hh} \right| kl \rangle h_i^\dagger h_j^\dagger h_k h_l. \end{aligned} \tag{2.18}$$

The operators c_i and h_i represent the electron and hole creation operators while those marked with a † represent the annihilation operators for the elelctron/hole in state $|i\rangle = |mn \updownarrow\rangle$ and the single particle energy $E_i^{e,h}$. $\left\langle ij \left| V_{\{ee,eh,hh\}} \right| kl \right\rangle$ are the two-body Coulomb matrix elements for electron-electron, electron-hole and hole-hole scattering (Hawrylak, 1999). The consequence of the Hamiltonian in equation 2.18 is that for every additional exciton that is generated, all interactions are altered, which gives rise to a new emission spectrum that can be used for detailed characterization of the dot.

Note also that the Coulomb interaction can be modified by applying an electric field which consequently alters the electron-hole distance and thus also the dipole moment. This also results in a modified emission spectrum. We shall return to this effect later and discuss it in further detail.

2.3 Carrier relaxation mechanisms

Unlike bulk systems where a continuum of states exist for carriers to relax or be excited to, the discrete nature of a QD is much more restrictive. Due to the discrete nature of the QD states, the usual phonon relaxation mechanism known for bulk materials is unlikely to happen, because a phonon with an energy closely matching the QD energy spacing itself is very unlikely. This results in slow relaxation to the ground state and makes radiative emission from the QD ground state unlikely as well. This scenario is known as the phonon bottleneck. However, other relaxation mechanisms exist that can bypass the phonon bottleneck and allow for efficient luminescence of QDs.

Assume that electrons and holes – created for instance by optical or electronic pumping – exist in the bulk continuum surrounding the QD. The charge carriers quickly relax into the wetting layer and shortly thereafter into the highest QD state. This process happens on a picosecond timescale and further relaxes through the lower lying QD states until the ground state is reached. This most likely happens via the repeated emission of two LO phonons or via electron-hole scattering processes as described by Müller et al. (2003).

Provided that an optical transition is allowed, an exciton can also radiatively recombine or an electron can also relax from state to state via emission of a low energy photon. Alternatively, phonon interactions and Auger processes are also possible but non-radiative relaxation mechanisms.Furthermore, the dephasing mechanisms are related to the relaxation processes and the homogeneous broadening of the QD emission line, while the homogeneous linewidth Γ is proportional to the exciton lifetime related relaxation and scattering rates

$$\Gamma \propto \frac{\hbar}{\tau} \text{ with } \frac{1}{\tau} = \sum_i \frac{1}{\tau_i}. \tag{2.19}$$

Acoustic phonon interactions are mainly the result of deformation potential coupling. The deformation potential is the result of the lattice vibrations caused by the phonon, which consequently modulates the lattice constant and thus the local electronic structure

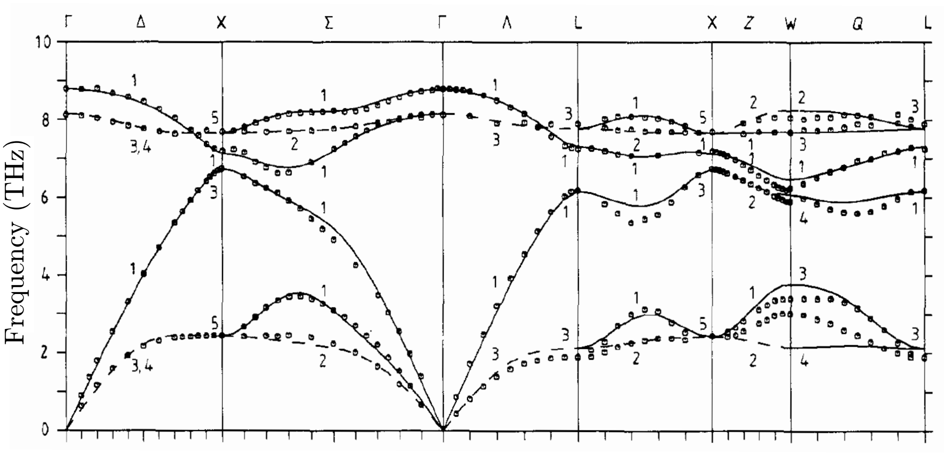

Figure 2.3: Measurement (circles) and model (lines) of the optical and acoustic phonon dispersion relation in GaAs at 12 K for various symmetry directions reproduced from Strauch and Dorner (1990).

of the crystal. This local modification of the electronic structure functions as a low energy (usually a few meV as can be seen in figure 2.3 for GaAs) scatter mechanism and becomes more inefficient as confinement increases. It is also noteworthy that this process is more inefficient for electrons than for holes due to the higher confinement they experience because of their lower effective mass.

Optical phonon interactions can be attributed to Fröhlich coupling of LO phonons and charge carriers. Fröhlich coupling is the coupling of the electric field created by lattice vibrations of an ionic crystal with the Coulomb field of an optically excited exciton (Woggon, 1996). While this process is the dominating relaxation process in quantum wells it is very unlikely to happen in QDs, as the phonon energy has to overlap with the energy spacing of the dot.

Seen independently, the optical and acoustic phonon interactions are a very inefficient and slow relaxation process in dots due to the phonon bottleneck[1].This, however, contradicts many observations of highly luminescent QD ground states because so far it has been assumed that only single phonon interactions occur. If multiphonon processes are considered, the picture changes and efficient relaxation becomes possible. For multi-

---

[1] It has recently been found however, that this is only valid for energy spacings less than the LO phonon energy. For greater energy spacings, polaron anharmonicity becomes a fast relaxation mechanism. Further details and theory can be found in Grange et al. (2007, 2009).

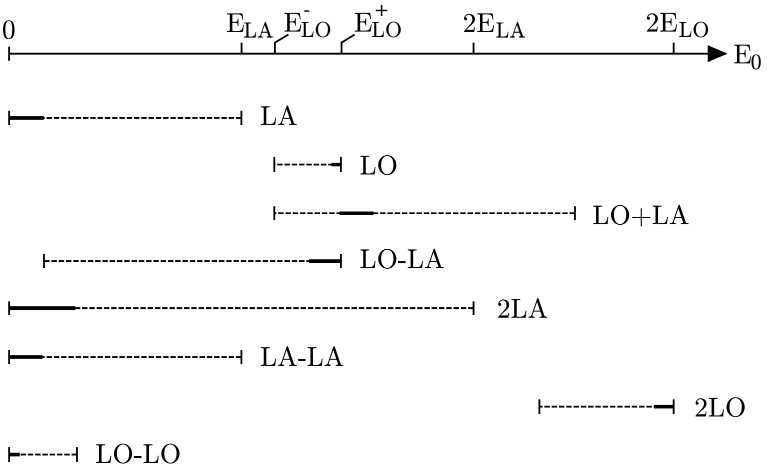

Figure 2.4: Schematic of the possible multiphonon processes reproduced from Inoshita and Sakaki (1992). E_0 is the QD level spacing with E_{LA} marking the maximum LA phonon energy, E_{LO}^{-} marking the minimum (zone edge/L point) and E_{LO}^{+} the maximum (zone center/Γ point) LO phonon energy with efficient relaxation being marked by thick lines.

phonon processes, relaxation rates are expected to be within the picosecond range, which – when compared to the radiative relaxation rate of ~ 1 ns – allows for efficient radiative relaxation. Figure 2.4 shows efficient and possible multiphonon relaxation energies for varying QD level spacing as described by Inoshita and Sakaki (1992).

Auger processes are a further non-radiative relaxation mechanism that allow an efficient bypass of the phonon bottleneck. This multi carrier process allows for relaxation by exciting a second carrier to a higher state or even into the continuum, and is predicted to be very quick. A relaxation time of $0.07 - 10$ ps has been predicted by Ferreira and Bastard (1999), which is even quicker than the multiphonon process described before. Fiore et al. (2000) observed the process take place on the timescale of 10 ± 2 ps in InAs/InGaAs QDs.

As for radiative relaxation mechanisms, intraband transitions can also occur radiatively and have been observed by Sauvage et al. (1999) with relaxation times in the μs range. Thus, this is a very inefficient process but can nevertheless be useful in applications where low photon counts are desirable. The aforementioned interband radiative exciton relaxation takes place in the ns range (Fiore et al., 2000) and is therefore more interesting for applications where higher output power and higher photon counts are required.

2.4 Electronic control of Quantum Dot states

At the end of section 2.2 the possibility of modifying the dipole moment of the Coulomb interaction by applying an electric field was briefly mentioned. We will now return to this phenomenon and discuss it in more detail since it is fundamental to this thesis. In order to account for an electrical field **F**, an additional potential

$$V_F(\mathbf{r}) = -e\mathbf{F} \cdot \mathbf{r} \tag{2.20}$$

needs to be added to the Hamiltonian. The addition of the potential 2.20 has several effects. Firstly, the wave functions of the electron and hole are altered due to the new potential configuration. Secondly, the electron and hole are pulled apart, increasing the dipole moment. And thirdly, forcing the electron and hole further apart also decreases their wave function overlap thus decreasing the oscillator strength. The overall effect of the additional field is a red shift of the QD emission, which is called the Stark shift while this phenomenon is known as Quantum Confined Stark effect or briefly the Stark effect.

According to Miller et al. (1985), for a quantum well, the Schrödinger equation can be written as

$$-\frac{\hbar^2}{2m^*}\frac{d^2}{dz^2}\xi(z) - (W + eFz)\xi(z) = 0 \tag{2.21}$$

with the component of the electric field in growth direction F, the eigen energy W and the wave function $\xi(z)$. The zero field solutions W_n and $\xi_n(z)$ are known and are usually assumed to be the solutions of the infinitely deep well since they provide a good and sufficiently accurate insight without too complex calculations. At this point one can either seek an accurate analytical solution and solve the Airy differential equation as according to Miller et al. (1985) or use perturbation theory with the approximation for weak fields

$$eFL \ll \frac{\hbar^2\pi^2}{2m^*L^2} \tag{2.22}$$

as done by Bastard et al. (1983). The small field approximation is justified for instance when $F \ll 60$ kV/cm in a 10 nm quantum well with $m^* = m^*_{e,GaAs}$. The weak field approximation yields the energy shift

$$\Delta E_1^{(2)} = -\frac{1}{24\pi^2}\left(\frac{15}{\pi^2} - 1\right)\frac{m^* e^2 F^2 L^4}{\hbar^2} \tag{2.23}$$

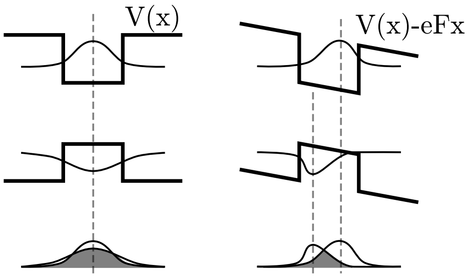

Figure 2.5: Schematic of the altered wave functions for an applied field and their reduced overlap.

which is only the second-order perturbation correction term since the first-order correction vanishes for symmetrical wells. This result is interesting as one can see that the Stark shift depends strongly on the electric field and even stronger on the size of the well. However, if the size of the well or the field become too large, as mentioned before, this approximation becomes invalid and one has to use a variational approach as used by Bastard et al. (1983) or Miller et al. (1984), or solve the problem analytically. For later measurements the Stark shift curves can be parametrized as follows

$$E(F) = E_{1,0} + \Delta E_1^{(1)} + \Delta E_1^{(2)} = E_0 + \alpha F + \beta F^2 \tag{2.24}$$

with the zero-field ground state energy $E_{1,0}$, the dipole moment α for the first order correction in order to account for the asymmetric case, and the polarisability β to account for the second order correction.

Another result of the perturbation theory approach is the correction to the wave function which shifts the expectation values away from each other and reduces the overlap. The decreased overlap also decreases the oscillator strength and the emission becomes weaker (Polland et al., 1985). In addition, a weaker oscillator means a lower recombination rate and thus a homogeneous broadening of the emission line. The alteration of the wave functions and the reduced overlap is schematically illustrated in figure 2.5.

The model mentioned above, however, is for quantum wells and lacks some detail where QDs are concerned. Several unexpected effects for InAs QDs – which are also the type of dots the experimental part of this thesis will deal with – have been observed. It was found that the wave function centers of electrons and holes in InAs QDs are shifted against each other even when no external field is applied. Contrary to theories that predicted holes to be localized beneath the electrons, Fry et al. (2000) were able to demonstrate the opposite and explained this observation with a non-uniform Ga incorporation in the InAs dots. The non-zero Stark shift at $F = 0$ kV/cm observed in photocurrent measurements was attributed to a built-in dipole moment with $r = 4{\pm}1$ Å due to the wave function shifts. Fry et al. (2000) also demonstrated the quenching of the oscillator strength with increasing field strength which was mentioned before in conjunction with figure 2.5. Furthermore, this non-zero Stark shift can be different for every dot due to slight differences in size and composition, which for instance can be used to distinguish individual QDs by finding their zero field wavelength. Since the zero field wavelength corresponds to a specific bias voltage, the dots can be resolved by finding their individual zero field bias.

Chapter 3

Experimental Methods

In this chapter, the experimental methods of probing single quantum dots used later on in this thesis will be discussed. Since measuring the Stark shift of single InAs quantum dots is the main focus of this work, the spectroscopic methods and single dot access will be treated in detail. Section 3.1 will explain how to optically access single quantum dots and discuss the necessary processing, section 3.2 will deal with photoluminescence spectroscopy, while section 3.3 and section 3.4 will detail photocurrent spectroscopy and transmission spectroscopy.

3.1 Sample structure and processing

Since the main focus of this thesis is essentially the spectroscopy of single quantum dots, it is necessary to discuss how to access single quantum dots and the required processing of the sample. The first option is to focus the pumping laser beam directly onto the dot and collect the light again through the same lens and pass it on to the measurement assembly. Now, self-assembled dot samples typically have a dot density of around 10^8 cm^{-2}–10^{11} cm^{-2}, which makes accessing a single dot optically very challenging as the densities correspond to 1 μm^{-2}–100 μm^{-2} with the latter value making single dot spectroscopy impossible when assuming a focus spot size of approximately 1 μm. One can overcome this issue by using a scanning near-field optical microscope (SNOM). However, another non-trivial problem arises if several experiments need to be done on the same dot and the measurement assembly is not perfectly stable. In fact, even the slightest misalignment or mechanical vibration can lead to losing the quantum dot. These issues can be

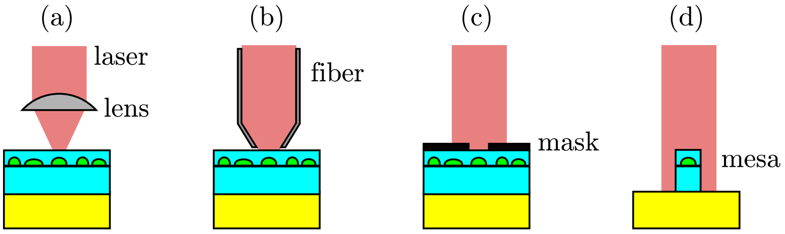

Figure 3.1: Optically accessing a single dot directly by focusing a laser beam (a), using a scanning near-field optical microscope (b), a mask with an aperture (c) or by etching a mesa and removing all other dots (d). The image was reproduced from Masumoto and Takagahara (2002).

overcome by either depositing a metal mask with small apertures on the sample or etching mesas with one dot inside. In both cases – when considering self-assembled quantum dots – it is unknown where the dots are located, and thus the fundamental assumption is if enough mesas are etched or enough apertures are placed, some mesas or apertures will contain a dot or have a dot beneath them. These single dot access techniques are summarized in figure 3.1.

For Stark shift measurements, principally all four access techniques are possible. However, due to the necessity of measuring the same dot repeatedly over a period of several months, directly focusing on the dot and SNOM are impractical. This leaves the latter two techniques, where masking the dots with a metal layer is well-suited for the application of a field parallel to the growth direction (vertical field) and etching a mesa is better suited for the application of a field orthogonal to the growth direction (lateral field). In this thesis the vertical field Stark shift is the main focus and thus masking the sample is the method of choice.

The quantum dot sample is a 350 μm ±25 μm SI-GaAs wafer used as substrate upon which a 300 nm layer of Si doped GaAs with a dopand density of $1.2 \cdot 10^{18}$ cm^{-3} was grown. All growth was performed at 490 °C. The 300 nm Si:GaAs layer will later function as the bottom electrode for Stark shift and photocurrent measurements. Upon the bottom electrode a 40 nm intrinsic GaAs layer is grown which will function as a substrate for the self-assembled InAs quantum dots. The quantum dots are grown using the Stranski-Krastanov growth mode. During QD growth the rotation of the sample was disabled in

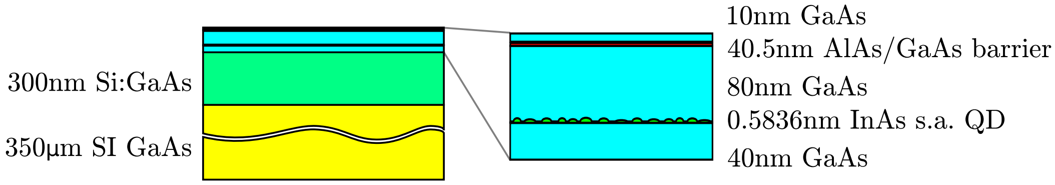

Figure 3.2: Upon a Si 350 μm ± 25 μm wafer a 300 nm layer of Si doped GaAs that functions as the bottom Ohmic contact followed by an intrinsic 40 nm GaAs layer is grown upon which InAs self-assembled QDs are fabricated. The QDs are then capped with 80 nm intrinsic GaAs layer, 27 layers of AlAs(5 Å)/GaAs(10 Å) and a final 10 nm GaAs layer.

order to achieve a non-uniform dot-density[1]. The InAs dots were then capped with further 80 nm of intrinsic GaAs. In order to prevent current from flowing through the sample, a barrier composed of 27 AlAs(5 Å)/GaAs(10 Å) layers followed by a final 10 nm GaAs layer were deposited. A schematic of the sample structure is shown in figure 3.2. The dots in this sample have a base diameter of 32 ± 5 nm according to AFM measurements and 31 ± 8.6 nm according to TEM. The height is 5 ± 2 nm (AFM) and 6 ± 1.5 nm (TEM) as measured for this sample by Fasching (2006).

In order to perform Stark shift measurements, first the bottom electrode had to be structured, followed by a semi-transparent Ti layer upon which the Au top contact with apertures is deposited. In order to form the bottom electrode, a 250 nm–300 nm high 4 mm×4 mm mesa was etched. The mesa was covered with a 5 mm×5 mm layer of photo resist for consequent Ge(15 nm)/Au(30 nm)/Ni(14 nm)/Au(200 nm) evaporation and lift-off to form the bottom contact around the mesa. Following the bottom contact, the top contact must be structured. The top contact is composed of a 5 nm Ti layer followed by a 100 nm Au layer with an array of aperture blocks as shown in figures 3.3 and 3.4. Before depositing the metal layers, however, surface defects had to be masked for later lift-off because measurements revealed that the surface defects were 250 nm deep and reached into the Si:GaAs layer[2]. An overview of the processing steps is illustrated in

---

[1] During material deposition, the sample is usually rotated in order to achieve a uniform layer, or in this case a uniform dot density which is usually in the range of 10^{10} cm^{-2}. However, a dot density of $\approx 10^{8}$ cm^{-2} $= 1$ μm^{-2} is desired, and is achieved on the outer regions of the wafer by turning off the rotation during dot growth.

[2] If the surface defects (holes) were filled with metal, they would connect the top and bottom contacts

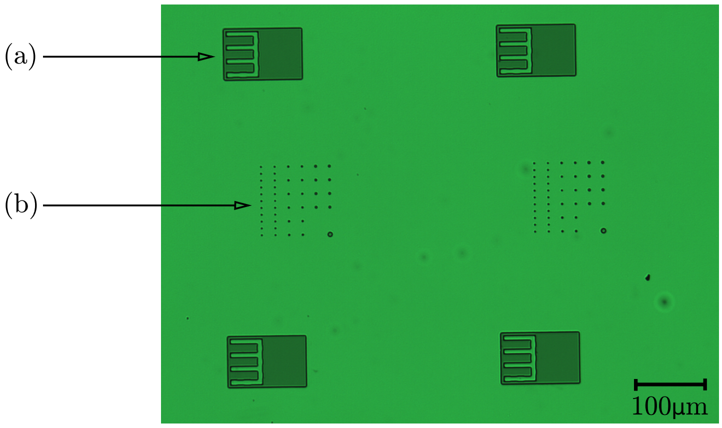

Figure 3.3: Photographic depiction of the aperture mask featuring alignment structures (a) with aperture blocks (b) composed of apertures with varying sizes as detailed in figure 3.4, placed at regular intervals.

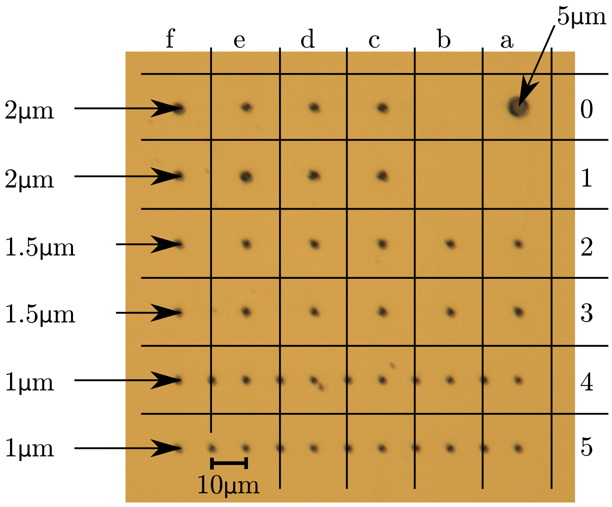

Figure 3.4: 100 nm Au aperture array structured on 5 nm Ti via lift-off with aperture sizes and naming convention col, row superimposed.

figure 3.5 while the resulting band structure of the sample including the top and bottom contacts is schematically illustrated in figure 3.6. Also note the Schottky type top contact and the Ohmic bottom contact. According to Fasching (2006) this results in a built-in potential of -0.55 V and has to be accounted for in the Stark shift measurements.

---

thus making Stark shift measurements impossible.

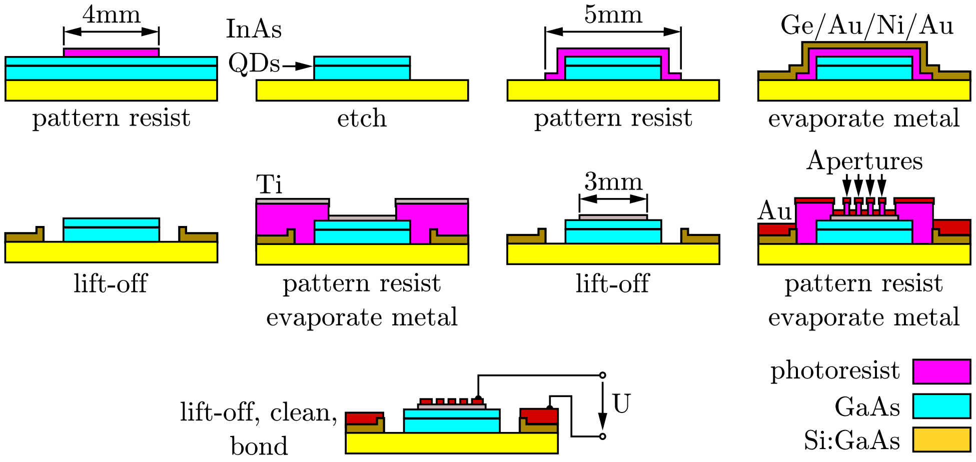
4mm
pattern resist
InAs
QDs
etch
5mm
pattern resist
Ge/Au/Ni/Au
evaporate metal
lift-off
Ti
pattern resist
evaporate metal
3mm
lift-off
Apertures
Au
pattern resist
evaporate metal
lift-off, clean,
bond
U
photoresist
GaAs
Si:GaAs

Figure 3.5: Brief progression of sample processing steps to fabricate the macro mesa with a top and bottom electrode. The top electrode also functions as a shadow mask.

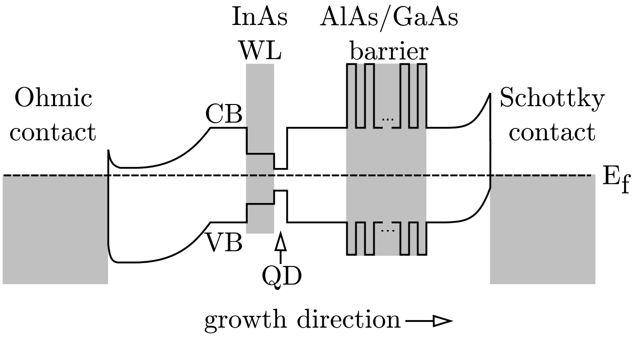
InAs
WL
AlAs/GaAs
barrier
Ohmic
contact
CB
Schottky
contact
E_f
VB
QD
growth direction

Figure 3.6: Schematic illustration of the band structure corresponding to figure 3.2 featuring the Ohmic bottom contact, the InAs wetting layer with embedded QDs, the AlAs/GaAs barrier and the Schottky top contact.

3.2 Photoluminescence spectroscopy

Photoluminescent (PL) spectroscopy is a very useful tool for analyzing the electronic structure of quantum dots. The principle is simple: excited carriers are generated by a beam of incoming photons. These carriers then relax under the emission of photons, corresponding to the possible radiative transitions of the system as discussed in section 2.1. The emitted light is then collected and passed on to a spectrometer for further analysis. If small systems – such as single quantum dots – are of interest, a focusing assembly can also be included in the setup. This is then referred to as micro photoluminescence or μPL spectroscopy.

The μPL spectroscopy setup used here consists of a HeNe laser and a Ti-Sapphire laser that can be individually selected as excitation sources via a mechanically actuated mirror. The HeNe Laser is a fixed wavelength laser from Spectra Physics, emits at 632.8 nm and has an optical output power of 15 mW. Due to its fixed short wavelength it is used as a non-resonant excitation source. The Ti-Sapphire laser is a Spectra Physics "3900S CW tunable Ti:sapphire Laser" and is pumped by a 5 W Spectra Physics "Millennia V Diode-Pumped, CW Visible Laser". With the current mirror set, the Ti-Sapphire can be tuned from 860 nm to 1000 nm with a bandwidth of 40 GHz (according to the specifications) and therefore is well-suited for resonant excitation, photocurrent spectroscopy as described in section 3.3 and transmission spectroscopy as detailed in 3.4. The optical output power of the Ti-Sapphire laser was measured to be between 100 mW and 200 mW depending on its output wavelength and decreases for growing wavelengths. Following the HeNe laser is a line filter that only allows the 632.8 nm line to pass. After the light source selection mirror is a neutral density filter that functions as an attenuator and allows control over the excitation power sent to the sample. The chopper is optional and not required for PL and μPL measurements when the CCD branch of the spectrometer is used. It is, however, required for the photocurrent and transmission spectroscopy experiments later on. The excitation beam is then collimated by two lenses and shaped by an iris aperture. The beam is then directed through a beam splitter to a "Carl Zeiss LD Achroplan 20x/0.40 Corr" objective that provides a 20x magnification and has a numerical aperture of 0.4 which results in a minimum beam diameter of

$$d = 2w_0 \approx \frac{2\lambda}{\pi\theta} \approx 1.55\ \mu\text{m with } \theta = \arcsin\left(\frac{\text{NA}}{n}\right) \tag{3.1}$$

for λ=1 μm photons and assuming the space in front of the objective is vacuum (i.e. $n = 1$) (Reider, 2004). The objective focuses the beam onto the sample that itself is located within a liquid helium cryostat from Oxford Instruments capable of lowering the temperature to 4.2 K. The cryostat is placed on a "Newport PM500" xy-stage in order to position a desired aperture directly in the focal point of the beam. The stage offers a resolution of 0.025 μm. The objective is placed on a linear optical stage in order to control the focus and for convenient removal of the cryostat.

The luminescence along with some reflected light from the excitation source is collected by the objective and is directed through the beam splitter and a “RG 750” long-pass 750 nm filter to the spectrometer. The long-pass filter is intended to suppress the reflected component of the HeNe excitation line when entering the spectrometer. The spectrometer is a Czerny-Turner design “Jobin-Yvon Spex 500M Research Spectrometer”. The spectrometer is essentially composed of two concave mirrors, an entry slit, a grating and an optical measurement device. The light is focused onto the entry slit which is seated in the focal point of the collimator mirror. The mirror then passes on a collimated beam to the diffraction grating. The diffraction grating then reflects the light, depending on its wavelength with an angle according to

$$\sin(\theta_{out}) = \frac{m\lambda}{\Lambda} + \sin(\theta_{in}) \tag{3.2}$$

where Λ is the grating period, m is an integer and $\sin(\theta_{in})$ can be seen as constant during a measurement thus resulting in $\sin(\theta_{out}) \propto \lambda$. The higher order reflections result in an increase in stray light within the spectrometer, which is why the inside walls are coated with absorbing material. The diffracted light is then collected and focused by the second concave mirror onto an exit slit if the spectrometer is used as a monochromator or onto an image recording device such as a CCD to record a full spectrum at once. Note, however, that if recording a full spectrum with an image recording device, the spectrum is distorted which can lead to erroneous measurement results. In the setup used for this thesis, the image recording device is a “Roper Scientific Spec-10:100” liquid nitrogen cooled CCD array with 1340 × 100, 20 μm×20 μm pixels. A spectrum of approximately 40 nm is covered by the 1340 horizontal pixels while the average over each 100 pixel column is taken to increase SNR. Thus the resolution is determined by the CCD and is approximately 0.03 nm. The spectrometer can also work in a monochromator mode via an electro-mechanically actuated mirror that redirects the beam to a slit located on the side wall next to the CCD. The photons exiting the slit are then recorded by a photomultiplier tube where the spectral resolution is given by the resolution of the spectrometer and the opening of the exit slit. A basic schematic of this design can be seen in figure 3.7 and a schematic of the entire setup is illustrated in figure 3.8.

To measure the Stark shift in this setup, a voltage is applied to the sample via a “TTi TG2000 20MHz DDS function generator” and the according spectra are recorded via the “Roper Scientific 10:100” CCD array. Alternatively the spectra can also be recorded by using the photomultiplier tube in conjunction with the “Stanford Research Systems Model

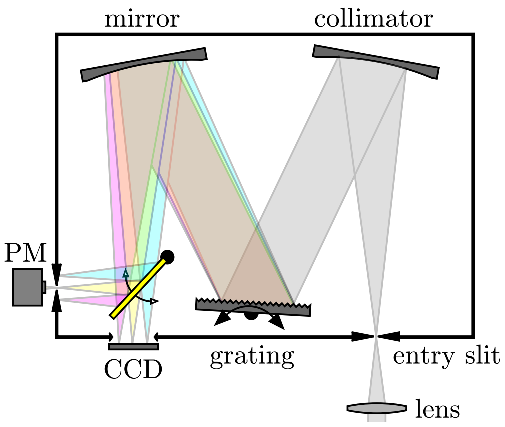

Figure 3.7: Schematic illustration of the Czerny-Turner spectrometer design.

SR830 DSP” lock-in amplifier and the chopper.

In addition to the spectrometer setup an optical microscopy branch has also been included in the setup. This branch is used for visual feedback while positioning the sample and focusing the excitation laser beam on the aperture. The additional branch is composed of a white light source and a CCD camera. By switching the mechanically actuated mirror in front of the white light source, either the laser beam or the white light can be sent to the sample thus allowing one to either view the sample under white light, or view the laser spot and adjust its focus – as long as the collected light is directed via the second mechanically actuated mirror to the CCD camera instead of the spectrometer.

Since the spectrometer, the Ti-Sapphire laser, the xy-stage, the lock-in amplifier and the function generator are all accessible via RS232 or GPIB, most of the measurement process could be automated. Using LabVIEW, the process of recording extensive spectra and Stark shift series was almost fully automated, allowing the room to be kept dark most of the time and thus preventing stray light from entering the spectrometer. This also reduced what was previously a set of several measurements required to record one longer spectrum to one single measurement, thus making the measurement process more efficient.

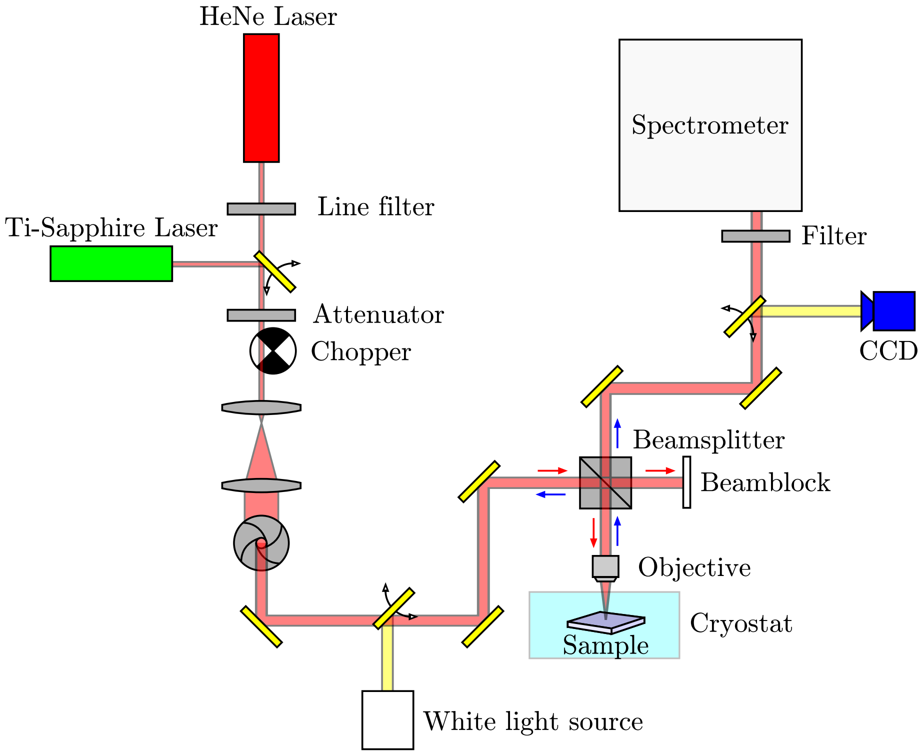
HeNe Laser
Line filter
Ti-Sapphire Laser
Attenuator
Chopper
Spectrometer
Filter
CCD
Beamsplitter
Beamblock
Objective
Cryostat
Sample
White light source

Figure 3.8: The laser source of the μPL setup is comprised of a HeNe and a Ti-Sapphire laser that can be individually selected via an electro-mechanically actuated mirror. The laser source is collimated and directed via a beam splitter to the objective which focuses the beam onto the sample. Light is also collected by the objective and passed on to the spectrometer. The filter before the spectrometer is used to remove the excitation laser line. An optional white-light path is also available for conventional microscopy, which is useful for positioning the sample.

3.3 Photocurrent spectroscopy

For the processed G677C sample two regimes were found. When a positive voltage is applied and the electric field points opposite to the growth direction, photoluminescence is observed. Conversely, for negative voltages, photoluminescence disappears and a photocurrent can be measured. The reason for this is that the applied field tilts the band structure such that the potential step at the dot barrier turns into a triangular potential through which particles inside the QDs can tunnel. Consequently, for a growing field strength, the barrier becomes thinner, resulting in a higher tunnel probability as shown in figure 3.9. If the tunnel rate, which is proportional to the tunnel probability, reaches the range of the radiative relaxation time, these mechanisms begin to compete. Finally if the field is increased even more, the luminescence becomes negligible as the generated excitons leave the dots before they can recombine, thus increasing the photocurrent. Note that this mechanism is tied to the generation of excitons and thus is linked to allowed optical transitions as discussed in section 2.1 and can therefore be used for spectroscopy by tuning the excitation wavelength.

As mentioned before, the Ti-Sapphire laser is useful for this experiment as it can be tuned from 800 nm to 1000 nm, which covers the range of QD emission from the G677C sample and thus will be used as an excitation source instead of the HeNe laser. Additionally, the sample needs to be biased and the photocurrent measured simultaneously. This can be accomplished using a pre-amplifier capable of biasing the input while passing on the amplified signal to a further lock-in amplification stage. Here a transimpedance pre-amplifier including a bias source was used. Figure 3.10 shows an idealized setup with an optically chopped light source for consequent lock-in measurement and the biased sample with the transconductance pre-amplifier. For this experiment two transconductance pre-amplifers of similar functionality were available. The first one, designed by Fasching (2006), is based on a low noise "Burr-Brown OPA 111" operational amplifier, provides a conversion factor of 10^8 V/A and allows for biasing of the sample with ±9 V (when 9 V batteries are used as a power source). The second pre-amplifier is an "Ithaco model 564 current preamplifier" with variable conversion factors ranging from $10^4 - 10^{10}$ A/V and biasing capability of 0 V to 10 V which, if directly connected to the sample, only allows a photocurrent measurement between 0 V and 0.55 V, which is only possible because of the -0.55 V built-in potential of the sample. Note also that conversion factors greater than 10^8 A/V can not be reached in the low noise mode.

3.4 Transmission spectroscopy

The basic idea behind transmission spectroscopy is that for every exciton generated, a photon is annihilated. The missing photons can be measured as a lower intensity of the beam that passed through the sample. In principle transmission spectroscopy relies on the detuning of the laser and QD levels while measuring the difference in transmission intensity. If the excitation laser is in resonance with a QD level, more photons are absorbed

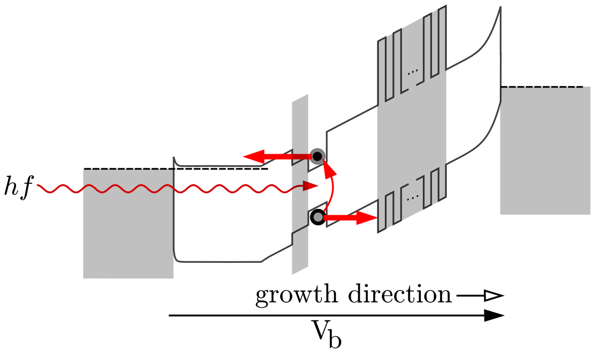

Figure 3.9: Schematic illustration of the sample's band structure with an applied voltage in the photocurrent regime. The photocurrent is induced by the tunnel barrier shortening.

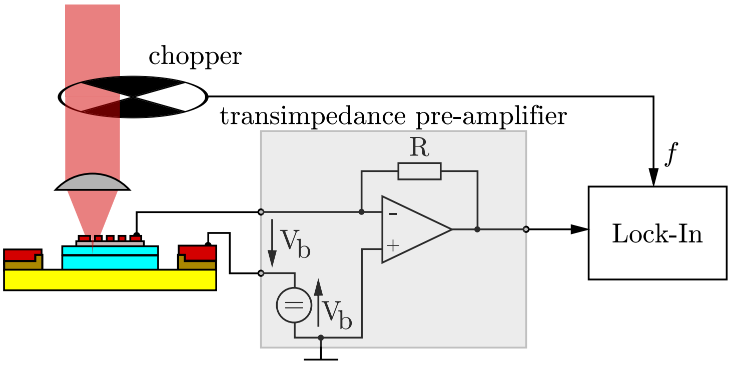

Figure 3.10: Idealized photocurrent measurement scheme.

by the dot and fewer photons exit the sample. When the laser is not in resonance with a QD level, no photons are absorbed and the beam ideally passes through the sample without any losses. Detuning can be achieved either by tuning the excitation laser line or by shifting the QD levels, which is where the Quantum Confined Stark Effect comes into play. The latter option is the option of choice, since tuning the excitation laser also affects the beam intensity and consequently leads to ambiguous results. The impact on the transmission intensity is expected to be higher when the sample is biased such that it is in the photocurrent regime since the excitons that contribute to the photocurrent are much less likely to recombine radiatively. For the photoluminescent regime the dots are expected to scatter the probing beam as generated excitons relax and emit photons in random directions. The impact upon beam intensity is, however, expected to be stronger in the photocurrent regime.

To perform transmission spectroscopy the setup explained in section 3.2 can be left mostly unchanged. The only difference is that the Ti-Sapphire laser is used as the excitation beam and that instead of with the spectrometer, the light is detected directly under the sample with a photodiode. The sample is then supplied with a low amplitude square wave with a variable DC offset. The offset is used to determine the DC component of the QD wavelength while the small square wave oscillates the states slightly. This has no effect until the QD line is in resonance with the excitation line. Then the small oscillation moves the lines into resonance and out of resonance at a known frequency, thus modulating the beam's intensity and can be detected by a lock-in amplifier.

The simplest and most efficient way to realize this setup is to simply stack the sample onto the photodiode. This allows for most efficient photon collection since the layer of vacuum between sample and photodiode is very thin and total internal reflection is frustrated. However, this results in two further problems. Firstly the photodiode, which is larger than the sample, collects stray light as well, which lowers SNR and – more importantly – allows for capacitive crosstalk between sample and photodiode even at very low frequencies due to the high amplification between photodiode and lock-in amplifier. This problem is made even worse as the crosstalk happens directly at the frequency at which the dot levels are modulated and are directly picked up by the lock-in. For example consider the case where the green line in figures 3.11(b) and 3.11(c) does not exist, then essentially a current is carried over $C_{gh} = C_4$ through the transconductance pre-amplifier – which ideally represents a virtual short circuit – back over $C_{ed} + C_{ef} = C_1 + C_2$. The resulting current can be calculated as follows

$$I = \frac{U_{in}}{2} \frac{\omega C_4 (C_1 + C_2)}{2C_1 + C_2 + C_4} \approx \frac{U_{in}}{2} \frac{\omega C_4 C_2}{C_2 + C_4}, \text{ with } C_1 \ll C_2, C_4. \tag{3.3}$$

Assuming

$$C_2 = C_{ef} = \frac{\epsilon_0 \epsilon_{r,Si} A_{\text{PD}}}{d_{\text{PD}}} = \frac{11.7\epsilon_0 (10 \text{ mm})^2}{635\ \mu\text{m}} \approx 16 \text{ pF} \tag{3.4}$$

for the capacity formed by the bottom contact of the photodiode with the cryostat chassis and assuming

$$C_4 = C_{gh} = \frac{\epsilon_0 \epsilon_{r,Si} A_{\text{sample}}}{d_{\text{sample}}} = \frac{11.7\epsilon_0 (8 \text{ mm})^2}{350\ \mu\text{m}} \approx 19 \text{ pF} \tag{3.5}$$

for the capacity formed by the sample's bottom contact with the photodiode's top contact one finds $I = \omega U 4.3$ pF which at 1 kHz, $U = 100$ mV and a conversion factor of $10^8\ \Omega$

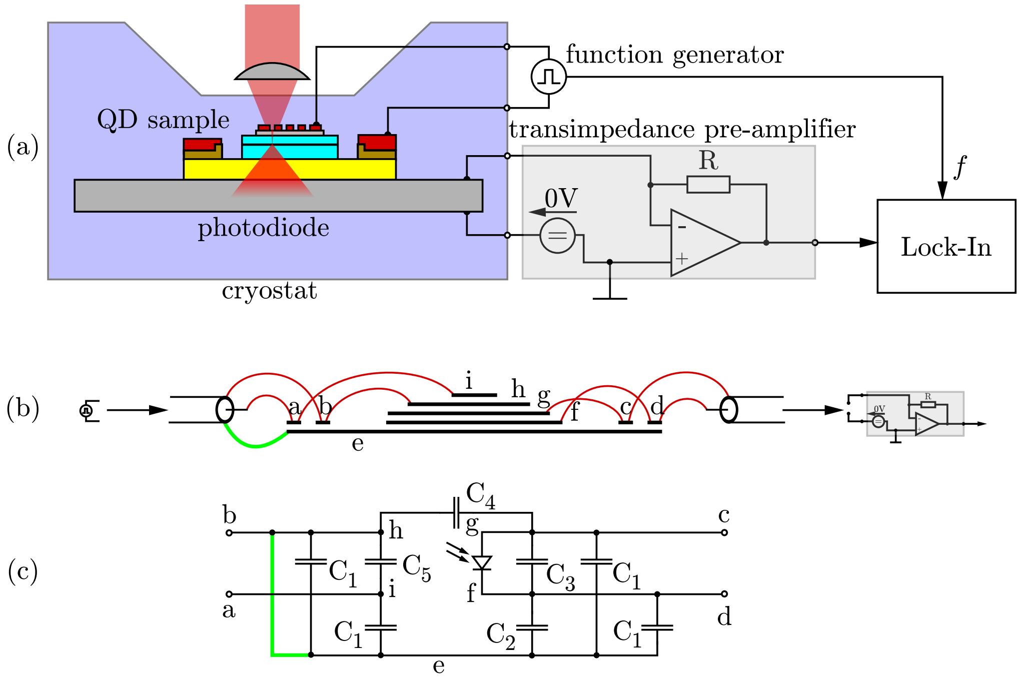

Figure 3.11: Idealized transmission spectroscopy measurement scheme without shielding of the photodiode (a), with the extracted electrode arrangement (b) and the corresponding parasitic capacity schematic (c). The green line is the connection of the cryostat with the shielding of the sample feed line. Note that the electrodes a, b, c and d have been assumed to be the same size and same distance from electrode e and thus all have the capacity C_1.

results in 273 mV at the lock-in input. Now, to compare this to the expected amplitude under ideal circumstances from the Stark shift modulation, a tunneling rate on par with a radiative recombination rate of 10^9 s^{-1} is assumed. It is further assumed that every photon generates one exciton that then contributes to the photocurrent. This results in a current of approximately 160 pA and equates to 16 mV at the lock-in. Even if the cryostat was grounded (green line in figures 3.11(b) and 3.11(c)), minute crosstalk – for instance from electrode i to g – would be sufficient to significantly degrade SNR. In fact without shielding we measured a peak value of 150 mV crosstalk at the lock-in when the grounding was removed. With grounding this value fell to 150 μV and initial shielding experiments lowered the figure to 30 μV. Furthermore under realistic circumstances an amplitude of 10^7 photons/s and a quantum efficiency of 80% are expected, which places the lock-in input signal at $10 - 100$ μV. This range is confirmed by similar measurements performed by Alén et al. (2003). Therefore shielding and proper grounding is imperative.

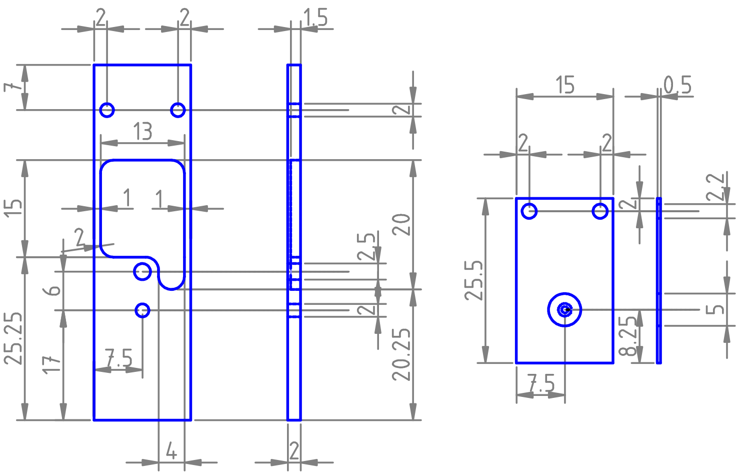

part A

part B

Figure 3.12: Blueprints of the milled photodiode shielding sample holder with the milled copper sheet (part A) and the copper cover plate with varying hole sizes (part B).

The problem was solved by using a $15 \times 55 \times 2$ mm^3 copper sheet and milling a 1.5 mm deep recess into which the photodiode is placed. This recess is then covered by a 0.5 mm thick copper cover plate with a 2 mm hole above the photodiode's center. Upon the hole, the QD sample with the aperture of interest is placed. This copper cover plate functions as an electrical shield for the photodiode while also almost completely shielding the photodiode from stray light. In this configuration, no crosstalk was detectable. Figure 3.12 shows the blueprints for fabricating the shielding and figure 3.13 shows a photo of the final sample holder setup with the shielded "FDS 1010 Si Photodiode" and bonded G677C sample.

With crosstalk under control, the issue of noise also needs to be addressed. Since low photon counts are dominant in this measurement scheme, shot noise will be an influential noise contributor. The shot noise current is given by

$$I_{shot} = \sqrt{2eI_0B} \tag{3.6}$$

with the elementary charge e, the photocurrent I_0, and the bandwidth B which is determined by the lock-in integration time. The photon density that needs to be supplied to the quantum dot for most efficient photocurrent generation is given by

$$\rho_{Ph} = \tau_{tunnel}^{-1} \sigma_{QD}^{-1} \tag{3.7}$$

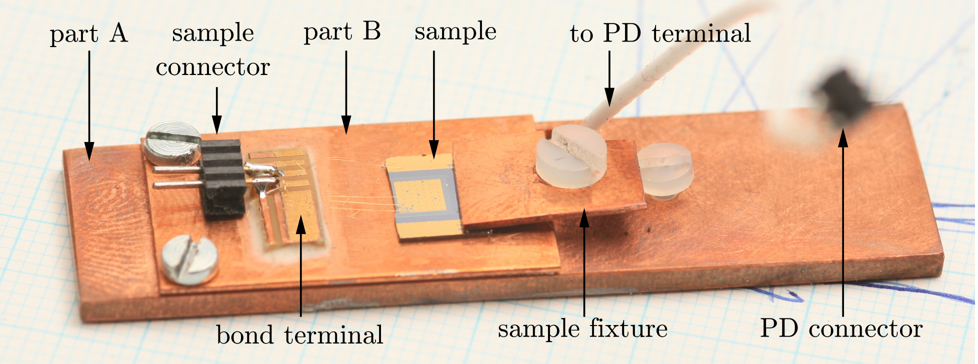

Figure 3.13: Photographic depiction of the final sample holder and photodiode (PD) shielding, capable of performing photoluminescent, photocurrent and transmission spectroscopy.

where τ_{tunnel}^{-1} is the rate of carriers tunneling out of the dot and σ_{QD} is the optical capture cross section which is proportional to the dipole length and will be assumed to be equal to $(0.18L_z/2)^2\pi$ as found by Sauvage et al. (1997a) and verified by Sauvage et al. (1997b) and Yu et al. (2005). In order to achieve ρ_{Ph}, a pump power of

$$P_{Pump} = \rho_{Ph} A_{aperture} \frac{hc}{\lambda} \tag{3.8}$$

is required at the sample and thus a laser power of

$$P_L = P_{Pump} \gamma_{path} \gamma \tag{3.9}$$

is needed. $A_{aperture}$ is the surface of the aperture above the quantum dot, λ is the excitation wavelength, γ is the inverse attenuation which is set on the attenuator in the setup and finally γ_{path} is the inverse attenuation the laser beam experiences when directed from the source to the sample, which in this setup equates to $\gamma_{path} \approx 10$. With these equations and the photocurrent $I_0 = e\eta_{PD}\frac{P_{Pump}}{hf}$ the noise at the lock-in can be calculated as follows

$$U_N = R_{CV} I_{shot} = R_{CV} \sqrt{2e^2 B \eta_{PD} \frac{A_{aperture}}{\tau_{tunnel}\sigma_{QD}}} \tag{3.10}$$

where η_{PD} is the external quantum efficiency of the photodiode and R_{CV} is the conversion factor of the transconductance pre-amplifier. Plugging in $\tau_{tunnel} \approx 1$ ns as an upper limit for the noise estimation, an optical capture cross section of $\sigma_{QD} = (0.26\text{ nm})^2\pi/4 = 5.3 \cdot 10^{-16}\text{ cm}^2$,[3] a bandwidth $B = 0.2$ Hz corresponding to an integration time $T_{int} = 5$ s, a quantum efficiency $\eta_{PD} \approx 0.87$ extracted from the data sheet and using an aperture with $A_{aperture} = (1.5\ \mu\mathrm{m})^2\pi/4$, the noise level at the lock-in equates to $U_N = 15.2$ mV. This illustrates how carefully the balance between excitation power density and noise needs to be considered when resonant excitation is concerned[4]. For a required SNR the necessary bandwidth can be calculated from equation 3.10, the signal amplitude $U_S = R_{CV} I_s$ and signal photocurrent $I_s = e\eta_{PD}/\tau_{tunnel}$ as

---

[3] Here a dipole length of 0.26 nm was found by Fasching (2006).

$$B = \frac{(U_S/\mathrm{SNR})^2 \sigma_{QD} \tau_{tunnel}}{2R_{CV}^2 e^2 \eta_{PD} A_{aperture}} = \frac{\eta_{PD}\sigma_{QD}}{2\mathrm{SNR}^2 A_{aperture}\tau_{tunnel}}. \tag{3.11}$$

Furthermore the inverse attenuation

$$\gamma = \frac{P_L \sigma_{QD} \tau_{tunnel}}{hf \gamma_{path} A_{aperture}} \tag{3.12}$$

which is gained from equations 3.9, 3.8 and 3.7 should also be known before the experiment is started.

---

[4] Note, that for PL spectroscopy this is not an issue, since not the optical capture cross section but the electron capture cross section is relevant, as electrons are captured from the bulk rather than being generated resonantly. The difference becomes clear when both cross sections are compared to each other. The electron capture cross section is orders of magnitude larger than the dot cross section (Engström et al., 2004), while the optical capture cross section is almost one order of magnitude smaller.

Chapter 4

Measurements and Discussion

4.1 μPL measurements

The photoluminescent measurements were carried out using the setup as described in section 3.2. The sample was fixed onto the sample holder as outlined in section 3.4 and mounted in the cryostat. The cryostat was then evacuated to 10^{-5} bar and then cooled to 5 K with liquid helium. The CCD was cooled with liquid nitrogen to -100 °C. The HeNe laser was used as the excitation source.

4.1.1 Quasi-ensemble aperture

The attenuator was set to 10^2 and the focus was set on the 5 μm aperture of the aperture block located at the center of the sample, which is approximately at (x,y)=(1525 μm, 1640 μm). This is the aperture a0 following the definition given in figure 3.4. Note that (0 μm, 0 μm) is the lower left corner of the top electrode where the bottom is defined as the side where the bond terminal is located. The sample's electrodes were left unconnected and a full spectrum from 600 nm to 1000 nm was recorded in 40 nm intervals via the CCD and stitched together using a custom-made LabVIEW VI. The recorded spectrum is shown in figure 4.1. The CCD integration time was 10 s. The left inset shows the remaining intensity of the suppressed HeNe excitation line at 632.8 nm. The right inset shows an excerpt from 920 nm to 960 nm in which several narrow lines can be observed. This indicates that quantized luminescent states are present in the sample and are beneath the gap energy of the the surrounding GaAs bulk (870 nm at 300 K; 816 nm at 5 K). The

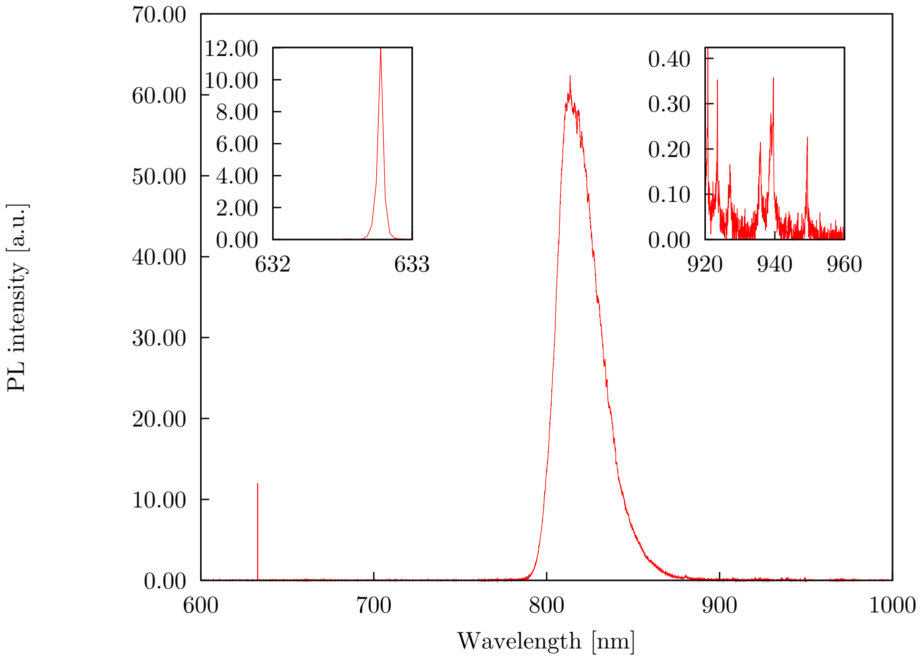

Figure 4.1: Measured spectrum from the 5 μm aperture a0 at 5 K. 63 mV was measured with the lock-in from the photodiode for the currently unknown excitation power density.

beam power P_{in} at the sample is expected to be 10 μW, which is the result of plugging $\gamma_{path} = 10$, $\gamma = 10^2$ and $P_{HeNe} \approx 10$ mW into equation 3.12. The attenuation γ is set at the attenuator after the excitation laser. Further, under ideal focus one can assume a laser spot size of $\pi(1.5\ \mu\text{m})^2/4$, and thus a power density of 566 W/cm^2 can be inferred. For further reference, the chopper was turned on and the photocurrent was measured from the photodiode via the “Ithaco 564” current preamplifier and lock-in to be 63 mV. This will be relevant for the next experiments, where an attenuator wheel – for which the attenuation is not accurately known – is used to perform excitation power sweep measurements. This will also be used to calculate the beam diameter in the next experiment because the assumption that the beam diameter reaches the previously calculated 1.5 μm is probably too optimistic.

4.1.2 Single dot aperture

The attenuator was left at 10^2 and the focus was set on the aperture a2, which is a 1.5 μm aperture, in the same aperture block as in the previous measurement. Again, the sample's electrodes were left unconnected and a full spectrum from 600 nm to 1000 nm was recorded in 40 nm intervals. The recorded spectrum is shown in figure 4.2. The CCD integration time was set to 30 s. The left inset shows the remaining intensity of the suppressed HeNe excitation line at 632.8 nm. The right inset shows an excerpt from 920 nm to 960 nm in which three narrow lines can be observed. The chopper was then turned on and the photocurrent was measured from the photodiode via the "Ithaco 564" current preamplifier and lock-in to be 42 mV. The amplitude is lower than in the previous measurement because the focus in not perfect and the beam is partially masked by the aperture. Assuming that part of the beam is masked, the ratio of measured voltages which are proportional to the excitation power, can be used to estimate the actual beam radius as follows

$$d^2 = d^2_{aperture} \cdot \frac{63 \text{ mV}}{42 \text{ mV}} \tag{4.1}$$

which places the beam diameter at $\approx 1.84\ \mu$m instead of the ideal value of 1.55 μm expected from this setup as calculated with equation 3.1. Now using $P_{in} = 10\ \mu$W, $\gamma_{path} = 10$, an attenuation of 10^2 and a laser focus crossection of $\pi(1.84\ \mu\text{m})^2/4$, a power density of 376 W/cm^2 is inferred for this as well as the previous measurement. This approximation is justified as the distance of the aperture plane and the dot plane is approximately an order of magnitude smaller than the aperture itself. Thus it can be assumed that the dot plane is seated in the aperture plane and interference effects resulting from diffraction can be neglected.

The same measurement is then repeated with a variable attenuator wheel placed in the beam path directly after the 10^2 attenuator and is turned until the voltage measured at the lock-in is reduced by one order of magnitude. The spectrum is then recorded with the CCD integration time set to 100 s and can be seen in figure 4.3. The right inset now only shows two distinct narrow lines (the very narrow line is a measurement artifact from the CCD). With the lock-in a signal amplitude of 4.8 mV was measured. Thus the power density with which the sample is illuminated can be estimated as $376 \text{ W/cm}^2 \cdot \frac{4.8 \text{ mV}}{42 \text{ mV}} \approx 43 \text{ W/cm}^2$.

A comparison of the spectra in the range from 920 nm to 1000 nm of the previous two measurements is shown in figure 4.4 along with an excerpt from 920 nm to 960 nm of the raw CCD data in figure 4.5 to illustrate the hot pixels which usually occur at random positions during measurements with longer integration times.

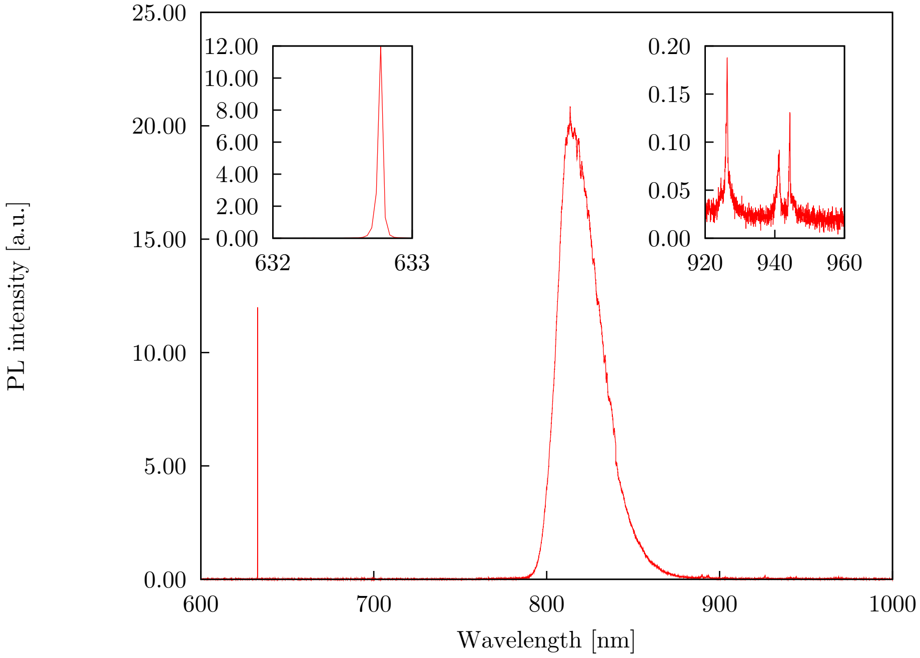

Figure 4.2: Measured spectrum from the 1.5 μm aperture a2 at 5 K and $P_{in} = \frac{10\ \mu\text{W}}{(1.84\ \mu\text{m}/2)^2\pi} \approx 376$ W/cm^2 and $T_{int} = 30$ s. The amplitude measured with the lock-in amplifier from the photodiode (42 mV) will be used as a reference for the 10^{-2} attenuation in 1.5 μm apertures.

4.1.3 Single dots under varying excitation intensity

For this measurement, the sample was kept at 5 K and the CCD integration time was set to 50 s. The laser was focused on aperture a2 and spectra were recorded for varying excitation power densities of 18 W/cm^2 (2 mV), 36 W/cm^2 (4 mV), 63 W/cm^2 (7 mV), 107 W/cm^2 (12 mV), 152 W/cm^2 (17 mV), 197 W/cm^2 (22 mV), 242 W/cm^2 (27 mV), 322 W/cm^2 (36 mV) and 358 W/cm^2 (40 mV) which were set by rotating the variable attenuation wheel. The wavelength range within which spectra were recorded was 900 nm–980 nm in 40 nm intervals. A gray-scale spectrogram assembled from the measurement data is shown in figure 4.6. The first four measurements and the last four measurements are arranged vertically from small power densities to large power densities and assembled in figures 4.7 and 4.8 respectively. Note the step-like change in PL intensity at exactly 940 nm for the high intensity measurements. This is the result of distortions in the border regions of the CCD which lead to stitching errors.

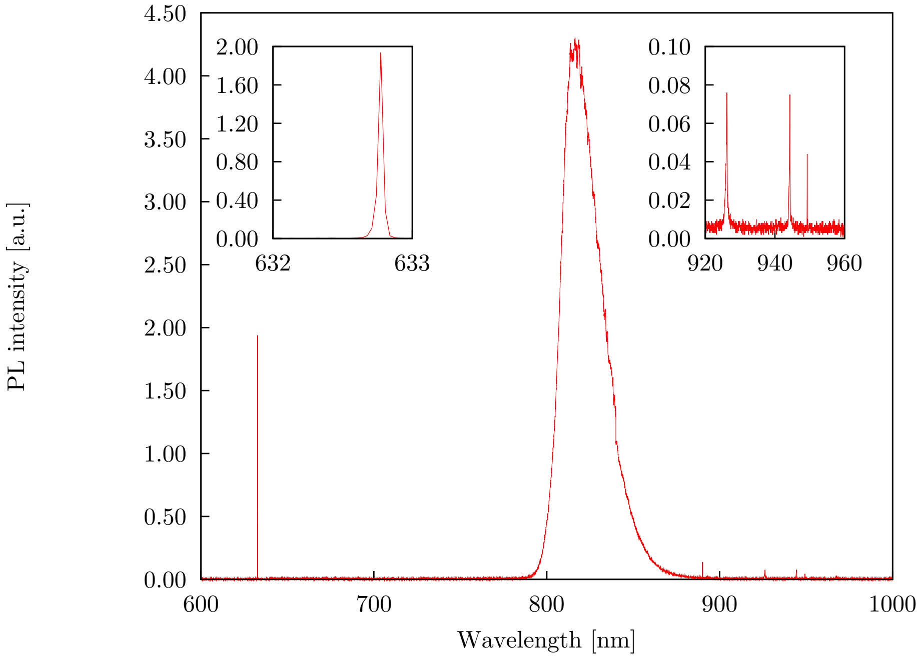

Figure 4.3: Measured spectrum from the 1.5 μm aperture a2 at 5 K and $P_{in} = \frac{4.8\ \text{mV}}{42\ \text{mV}} \cdot \frac{10\ \mu\text{W}}{(1.84\ \mu\text{m}/2)^2\pi} \approx 43\ \text{W/cm}^2$ and $T_{int} = 100$ s.

4.1.4 Discussion

The quasi-ensemble PL measurement served the purpose of demonstrating the existence of QDs in the sample, as was shown by the collection of distinct lines in figure 4.1. The measurement also served as a means to determine the beam diameter in the focal point with a further measurement on a 1.5 μm aperture. The determined beam diameter in the focal point allows for a more accurate calculation of excitation power densities that were used in the measurements thereafter.

The peak around 820 nm seen in figures 4.1, 4.2 and 4.3 is the luminescence of the bulk material. The luminescence tail for sub band gap energies observed for wavelengths >816 nm can be attributed to the Si doping of the GaAs bottom electrode (Kressel et al., 1968).

A comparison of single dot measurement results reveals that quantized states are present beneath the aperture a2. Furthermore, the result of the low intensity measurement suggests that three dots are present. The lines are also sufficiently far apart for them to be distinguishable. Therefore the presence of several dots will not hinder further single

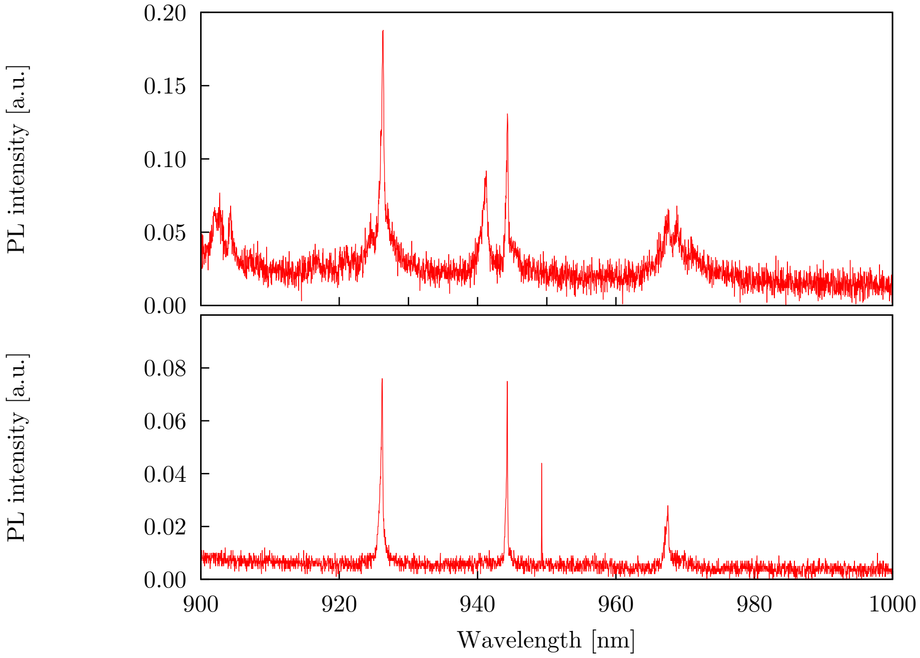

Figure 4.4: Comparison of the photoluminescence spectra from 920 nm to 960 nm for excitation power densities of 376 W/cm^2 (top) from figure 4.2 and 43 W/cm^2 (bottom) from figure 4.3. The peaks for the top spectrum are 926.43 nm, 941.35 nm, 944.40 nm, 967.59 nm and 968.84 nm. For the bottom spectrum the peaks are located at 926.30 nm, 944.36 nm and 967.56 nm. The narrow line at 949.33 nm is the result of a set of hot pixels.

dot measurements and further use of this aperture is justified.

By using line spacing data from similar measurements (Landin et al., 1998; Kaiser et al., 2002) it can be concluded that the lines emerging at 941.35 nm and 925.54 nm, for excitation powers greater than 100 W/cm^2, are excited states with their corresponding ground states located at 944.36 nm and 927.31 nm respectively. The line emerging at 968.84 nm beside the line 967.59 nm, which was also present at low intensity, is intriguing as it seems to be an excited state with a lower energy than the ground state. This can be explained by a multi-particle interaction as discussed in section 2.2 involving two electrons and one hole. This effect was also described and observed by Landin et al. (1998).

The narrow line at 949.33 nm is the result of an unusual set of hot pixels as this line did not appear in any preliminary measurements or the previous high intensity measurement. Additional evidence for this claim can be found in the raw CCD data in figure 4.5, where the peak values of the hot pixels are 311 and 583 counts while typical peak counts of 20-30

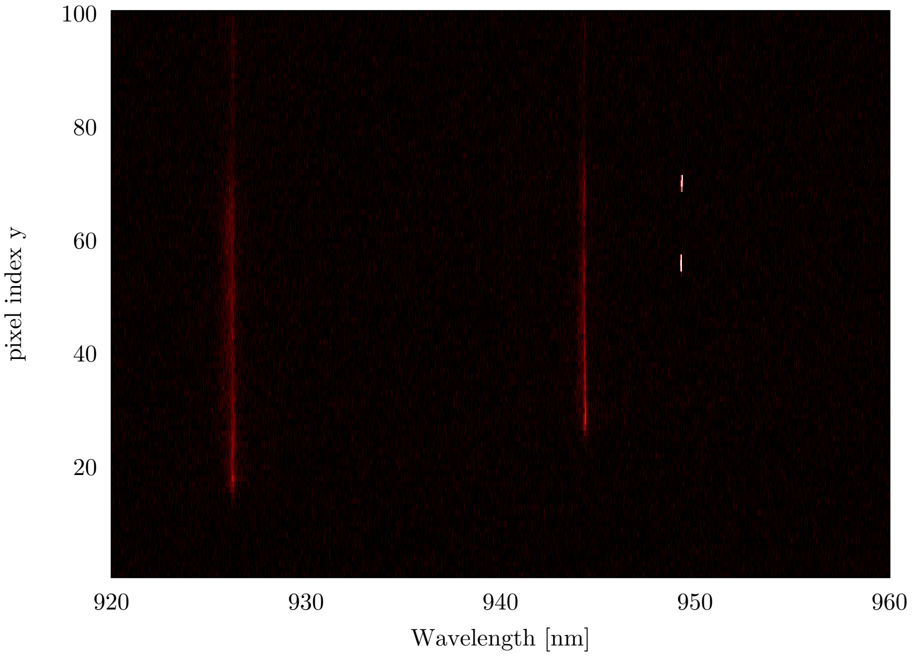

Figure 4.5: Raw CCD data from 920 nm to 960 nm of the 43 W/cm^2 measurement. The data was clipped at the lower end to 0 and at the higher end to 60 counts for better visibility. The peak value of the top hot pixel is 311 (x = 949.33 nm,y = 45) and 583 (x = 949.29 nm,y = 31) is the peak value for the lower hot pixel.

are observed within the elongated features which represent luminescent quantized states.

Finally it must be noted that the aperture structure did not permit measurements beneath $\approx 2W/cm^2$ as this would demand even higher integration times. Recording spectra at higher integration times, however, is difficult to achieve with this setup due to mechanical drift of the focusing stage and coupling of vibrations from the vacuum pump over the helium transfer line to the cryostat.

4.2 Stark Shift measurements

In order for this measurement to work, one needs to verify that the bond wires are actually connected to the sample. This was done by measuring the resistivity from the top to the bottom contact. At room temperature this value is 325 kΩ from the top to bottom contact and 2.5 MΩ with reversed polarity. At 5 K the resistivity in forward polarity grows to 728 kΩ and 8.2 MΩ in reverse. Unsurprisingly, the values also change depending on the

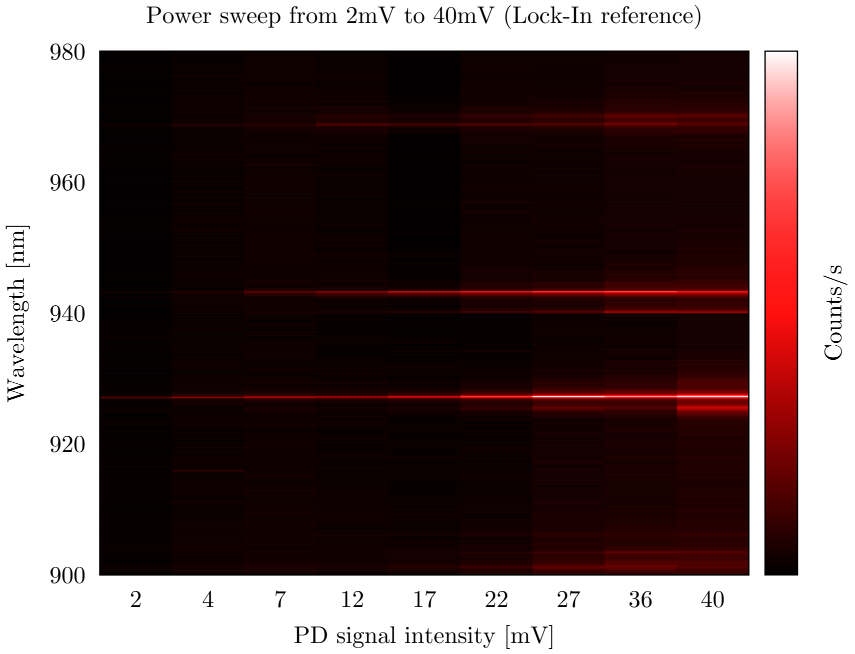

Figure 4.6: Power sweep from 18 W/cm^2 (2 mV) to 358 W/cm^2 (40 mV) for the wavelength range of 900 nm to 980 nm.

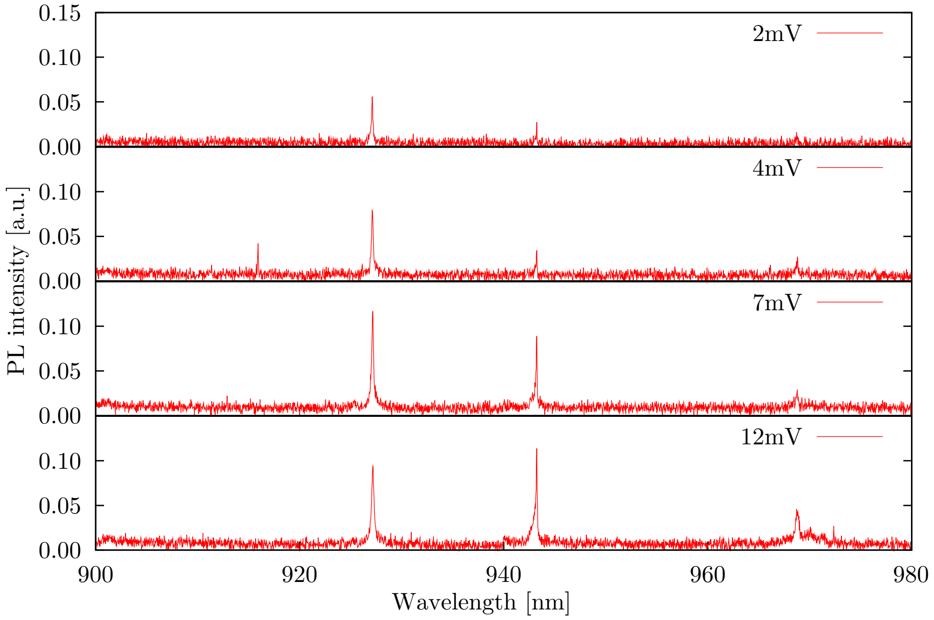

Figure 4.7: Spectrum from 900 nm to 980 nm for 18 W/cm^2 (2 mV), 36 W/cm^2 (4 mV), 63 W/cm^2 (7 mV) and 107 W/cm^2 (12 mV).

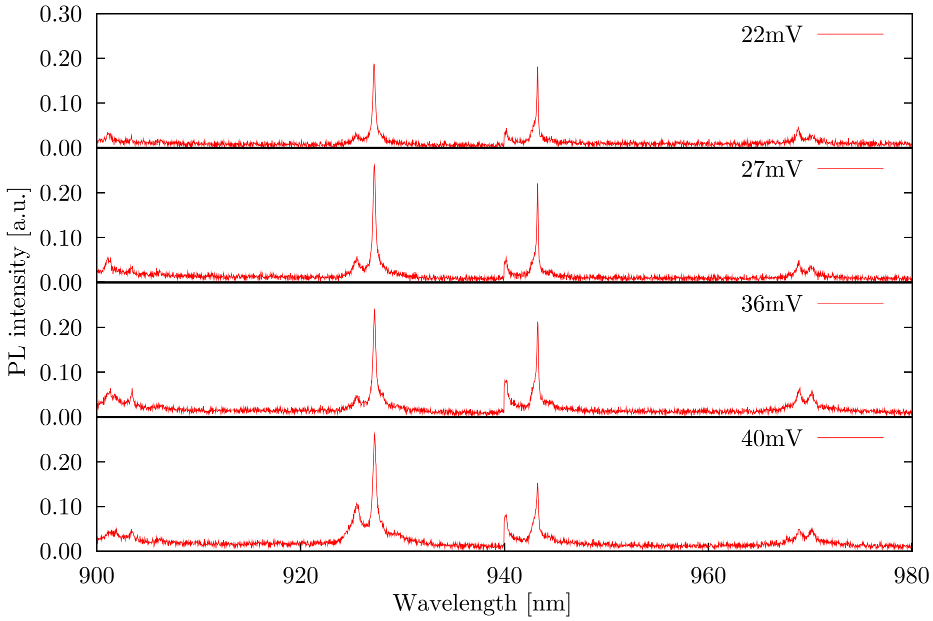

Figure 4.8: Spectrum from 900 nm to 980 nm for 197 W/cm^2 (22 mV), 242 W/cm^2 (27 mV), 322 W/cm^2 (36 mV) and 358 W/cm^2 (40 mV). Note that the step at exactly 940 nm is the result of stitching two 40 nm spectra with slightly distorted border regions.

illumination level.

The Stark shift measurements were carried out using the setup as detailed in section 3.2 while the sample was mounted in the cryostat as described in section 3.4. The sample was connected to “TTi TG2000 20MHz DDS function generator” and the photodiode was connected to the “Ithaco 564” transconductance amplifier which itself was connected to the lock-in. The cryostat was then evacuated to 10^{-5} bar and then cooled to 5 K with liquid helium. The CCD was cooled with liquid nitrogen to -100 °C and the HeNe laser was again used as the excitation source.

4.2.1 Stark shift under high excitation power

The focus was set on aperture a2 and the attenuation was set to 10^2 which equates to 376 W/cm^2 as in the previous measurements. The voltage was then set to 0.0 V and increased by 50 mV after recording a spectrum from 920 nm to 960 nm until 1.0 V was

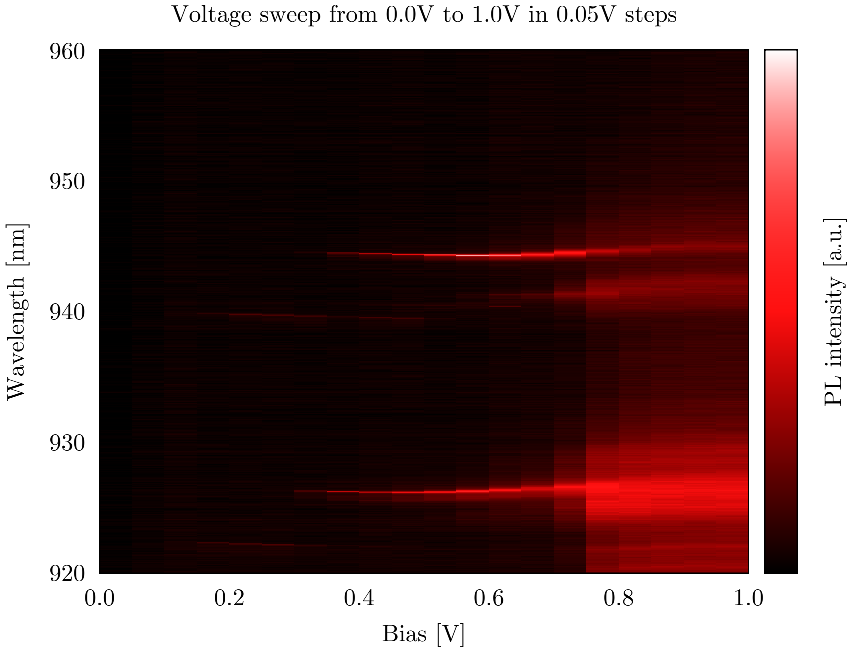

Figure 4.9: Voltage sweep from 0 V (-32.1 kV/cm) to 1 V (26.3 kV/cm) in 50 mV (2.9 kV/cm) steps in the range of 920 nm to 960 nm at 376 W/cm^2.

reached. Using

$$E = \frac{U - U_{Schottky}}{d} \tag{4.2}$$

this equates to fields from -32.1 kV/cm to 26.3 kV/cm in 2.9 kV/cm steps when considering the distance $d = 171.08$ nm from the top contact to the Si doped GaAs bottom contact and $U_{Schottky} = -0.55$ V from the Schottky contact's built-in potential. The resulting spectra as a function of the electric field are shown in figure 4.9 where darker shades represent higher intensities. Additionally, figure 4.10 shows the cross sections of figure 4.9 at 0.55 V (0 kV/cm), 0.65 V (5.8 kV/cm), 0.75 V (11.7 kV/cm) and 0.85 V (17.5 kV/cm) with the wavelengths of the peaks superimposed. The first line (926.30 nm at 0.55 V) shall be labeled lines A and the second line ($944.37nm$ at 0.55 V) shall be labeled line B. Finally, figure 4.11 illustrates the Stark shift of the lines A and B as a function of the electric field.

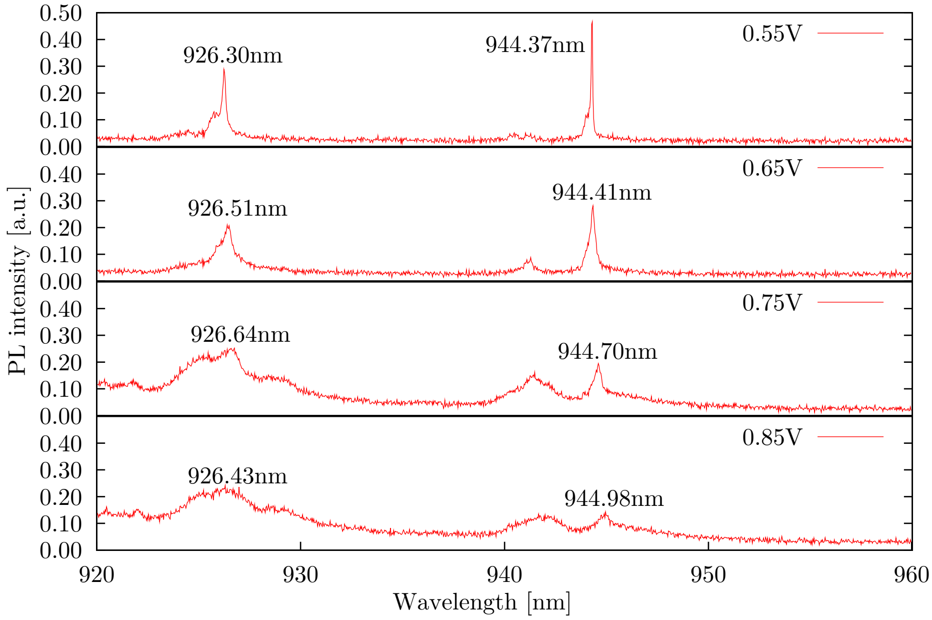

Figure 4.10: Spectra from 920 nm to 960 nm at 376 W/cm^2 for 0.55 V (0 kV/cm), 0.65 V (5.8 kV/cm), 0.75 V (11.7 kV/cm) and 0.85 V (17.5 kV/cm).

4.2.2 Stark shift under low excitation power

The focus was left on aperture a2 and the attenuation was reduced to 10^3 (38 W/cm^2). The voltage was then set to 0.2 V and increased by 25 mV after recording a spectrum from 920 nm to 960 nm until 0.9 V were reached. Using 4.2 the applied voltages equate to fields from -20.5 kV/cm to 20.5 kV/cm in 1.46 kV/cm steps. The resulting spectra as a function of the electric field are shown in figure 4.12. Figure 4.13 shows the cross sections of figure 4.12 at 0.55 V (0 kV/cm), 0.65 V (5.8 kV/cm), 0.75 V (11.7 kV/cm) and 0.85 V (17.5 kV/cm) with the wavelengths of the peaks superimposed as was done for the previous measurement. Figure 4.14 illustrates the Stark shift of the lines A and B as a function of the electric field.

4.2.3 Discussion

The high intensity measurement showed red-shifts of 0.45 nm for line A and 0.77 nm for line B. This equates to a Stark shift of 0.65 meV for line A and 1.07 meV for line B, which was calculated by using the well-known relationship $\Delta E = \Delta\lambda \frac{hc}{\lambda_0^2}$ with $\lambda_{0,A} = 926.30$ nm

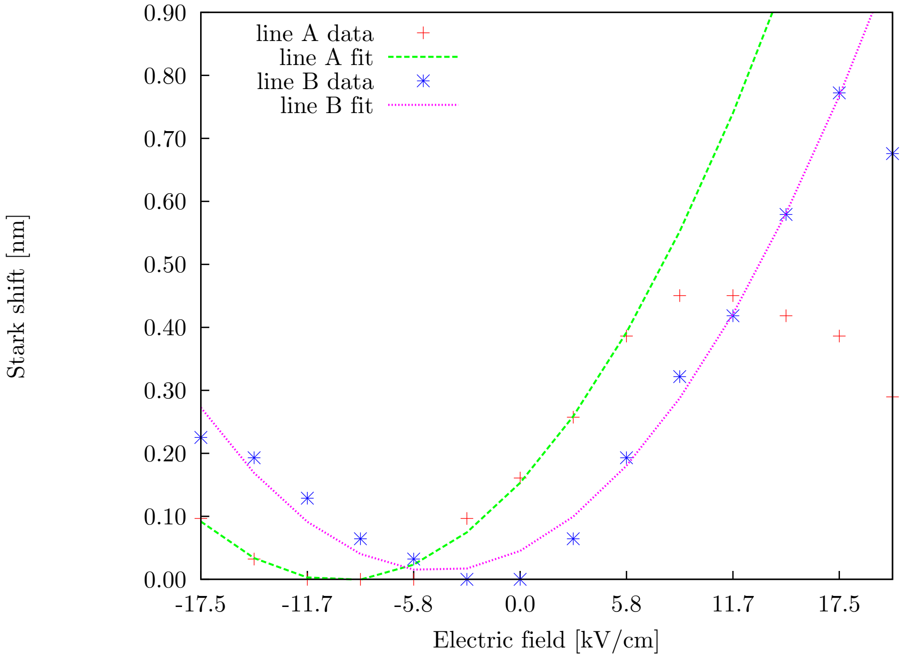

Figure 4.11: Stark shift as a function of the electric field under 376 W/cm^2 and curve fit with the parameters $\alpha_A = 5.138 \cdot 10^{-29}$ Cm, $\beta_A = 3.701 \cdot 10^{-35}$ CsT^{-1}, $\alpha_B = 1.130 \cdot 10^{-29}$ Cm and $\beta_B = 3.440 \cdot 10^{-35}$ CsT^{-1}.

and $\lambda_{0,B} = 944.37$ nm. The low intensity measurement showed red-shifts of 1 nm for line A and 0.71 nm for line B. This equates to a Stark shift 1.44 meV for line A and 0.99 meV for line B. Both figures 4.11 and 4.14 show that the Stark shifts of line A and B reach their minimum at different values of the electric field. From this two facts can be concluded. Firstly these lines indeed belong to two different QDs, and secondly, this is empirical evidence for the existence of a built-in dipole moment under zero field conditions as discussed in section 2.4. Additionally, since line A and B have been shown to belong to different dots, naming the dots dot A and dot B is also justified.

The high intensity measurements also show a lowering of the maxima and a broadening of the emission line for increasing fields which can be observed in figures 4.9 and 4.10. A possible explanation is that carriers are driven towards the wetting layer and are then captured by the wetting layer well, where they become additional Coulomb interaction partners for the carriers in the dot and alter the emission spectrum. The measurement integrates over all the altered states and a broadening can be observed. The lowering of the maxima is the result of broadening under the constraint of energy conservation which can

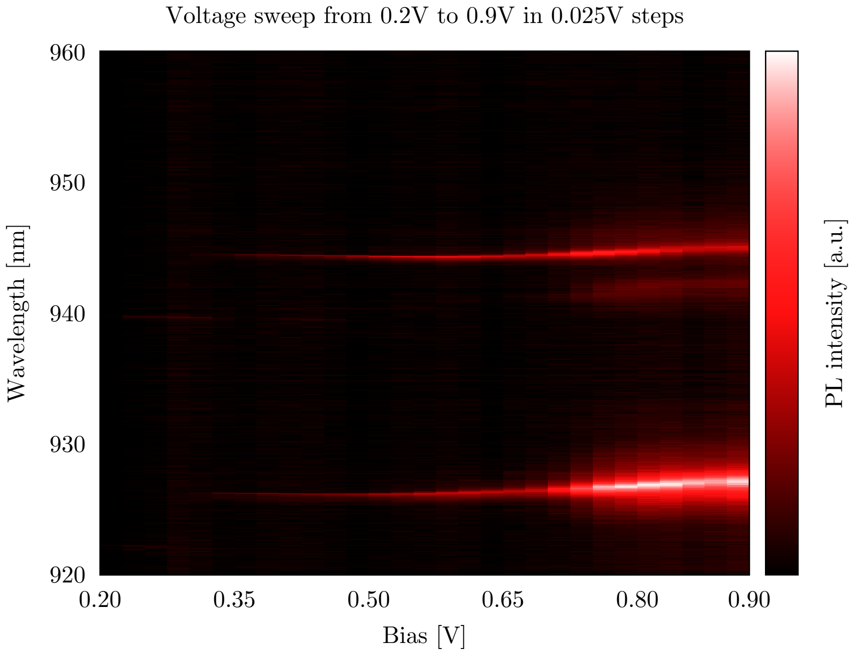

Figure 4.12: Voltage sweep from 0.2 V (-20.5 kV/cm) to 0.9 V (20.5 kV/cm) in 25 mV (1.46 kV/cm) steps in the range of 920 nm to 960 nm at 38 W/cm^2.

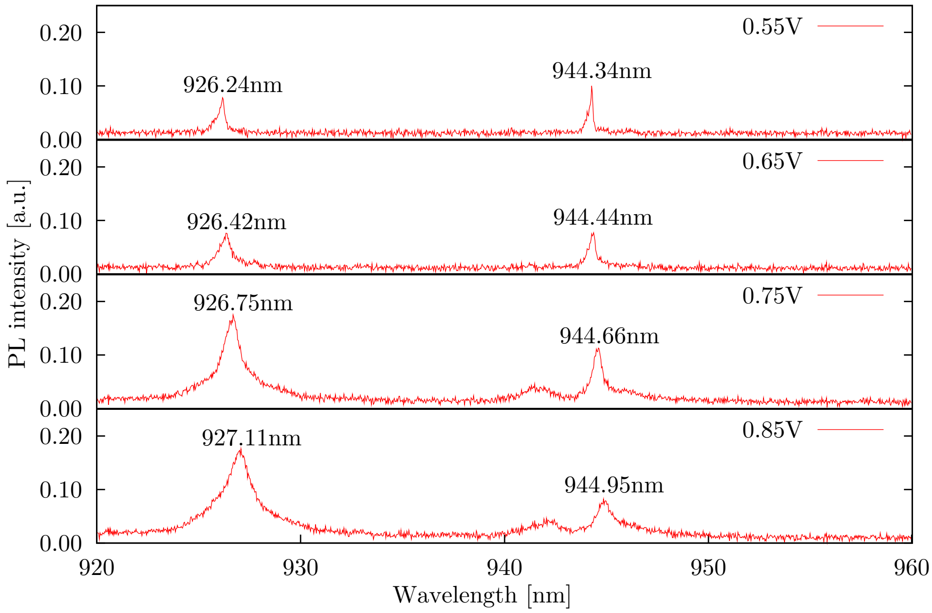

Figure 4.13: Spectra from 920 nm to 960 nm at 38 W/cm^2 for 0.55 V (0 kV/cm), 0.65 V (5.8 kV/cm), 0.75 V (11.7 kV/cm) and 0.85 V (17.5 kV/cm).

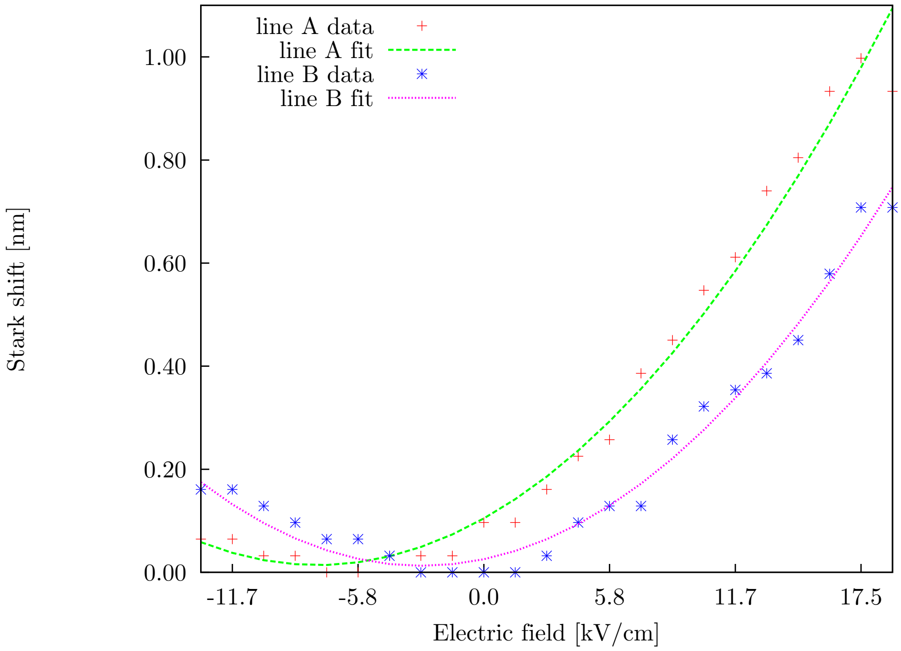

Figure 4.14: Stark shift as a function of the electric field under 38 W/cm^2 and curve fit with the parameters $\alpha_A = 4.392 \cdot 10^{-29}$ Cm, $\beta_A = 3.502 \cdot 10^{-35}$ CsT^{-1}, $\alpha_B = 9.690 \cdot 10^{-30}$ Cm and $\beta_B = 3.420 \cdot 10^{-35}$ CsT^{-1}.

be seen when the dots are in saturation as is the case in this high intensity measurement. For the low intensity measurements a different behavior is observed. Figures 4.12 and 4.13 show an increased broadening and luminescence intensity of the QDs. As was argued for the high intensity case, this can also be explained by increased carrier counts in the wetting layer for higher fields, which leads to line broadening due to the increased Coulomb interactions. However, since the dots are not yet in saturation, the higher carrier density in the wetting layer allows for more efficient carrier capture and luminescence.

Using

$$\Delta\lambda = \gamma F + \delta F^2 \tag{4.3}$$

as the fit polynomial, the fit parameters can be extracted from the Stark shift data, thus allowing further characterization of the QDs. The coefficient $\alpha = \frac{hc}{\lambda_0^2}\gamma$ represents the built-in dipole moment and the factor $\beta = \frac{hc}{\lambda_0^2}\delta$ the polarizability as discussed in section 2.4. High and low intensity measurements show similar values for α and β within the same dot, which is not particularly surprising. From α_A an electron hole separation of 2.7 Å under low illumination and 3.2 Å under high illumination can be inferred. This fits well with other measurements (Fry et al., 2000; Fasching, 2006). Similarly, from α_B electron hole separations of 0.6 Å (low excitation) and 0.7 Å (high excitation) were calculated.

The similarity of β_A and β_B seems to verify that the dots are similar in size as long as similar composition (i.e. $m_A^* \approx m_B^*$) can be assumed. Theoretically from β, also the size of the dots could be inferred, however, a more detailed QD Stark shift model is required to perform this accurately.

A fit in accordance with equation 4.3 for the excited states with the present measurement data is not possible since they only show luminescence for fields far from the zero field point.

Conclusions

In this work, quasi-ensemble measurements were carried out which showed that QDs in sufficient density were present on the sample. As a result, single dot spectroscopy was performed in order to find a suitable position for further measurements. An aperture containing two sufficiently bright QDs in the center of the sample was used to carry out Stark shift measurements. The simultaneous measurement of two well-distinguishable QDs was shown to be advantageous as this provided the means to better analyze the structure of single QDs. During these measurements it was verified that indeed a permanent dipole is present in InAs QDs and that this dipole can vary from dot to dot. The dipole lengths were extracted from the Stark shift data which can be used for consequent transmission measurements, as it is expected to be tied to the optical capture cross section (Sauvage et al., 1997a,b; Yu et al., 2005). Furthermore the polarizability of the dots was determined from the Stark shift data and was almost the same for both dots, which verified that the dots were similar in size when the composition is assumed to be similar.

In preparation for these measurements, several LabVIEW VIs were created that allow for more efficient and extensive μPL spectroscopy, Stark shift and transmission measurements when used in conjunction with the currently implemented setup. These tools remove the burden of micromanaging some trivial aspects of the setup and allow the user to concentrate on the actual measurement instead. Tools were written for CCD temperature monitoring, CCD data acquisition and post processing such as recording and stitching several spectra to create one large spectrum or allow the recording of spectrograms as done with the Stark shift measurements. These tools will provide a platform for efficient sample characterization as well as further transmission measurements.

The sample that was processed for this thesis was also designed along with a new sample holder to allow for transmission and Stark shift assisted transmission spectroscopy. The sample holder was designed to electronically shield the photo detector from the sample as crosstalk is an issue in such low current regimes. The sample holder also provides shielding from stray light which should also improve SNR.

All the designs and measurements in this thesis were carried out in preparation for Stark shift assisted single dot transmission spectroscopy. However, this method of spectroscopy still presents several challenges that need to be overcome. Precise control over noise and crosstalk needs to be maintained while accurately controlling the excitation power. Here a compromise between sufficient excitation power while keeping shot noise – which is proportional to the square root of the photocurrent – low is necessary. Also, in preparation a photocurrent spectrum needs to be recorded in order to position the Ti-Sapphire laser line correctly. Finally, the focus size and position need to remain constant while determining the correct excitation intensity. These issues require a redesign of the current setup to enable Stark shift transmission spectroscopy.

Acknowledgements

I would like to thank everyone who aided and supported me during the course of this work. Firstly, I would like to thank Karl Unterrainer, who kindly allowed me to join his group and provided me with all the necessary facilities to complete this thesis. Then I would like to thank my supervisors – Michael Krall, who spent many hours with me in the cleanroom and in the lab assisting me with my experiments, and Wolfgang Parz, who always had the time to help me with the setup and provide a warm cup of tea or a fresh bottle of very cool helium. I would also like to thank Thomas Gebhard and Thomas Moldaschl for literature, special equipment and many fruitful and genuinely fun discussions. I would like to thank Juraj Darmo for sharing his insight and advice with me on several occasions.

All the colleagues and friends that have not been mentioned thus far, I also thank them for all the help they gave me and all the fun I had with them.

On a more personal note, I want to thank my mother, Elizabeth, for everything she has done for me. Without her dedication and loving support, none of this would have happened. I would also like to thank my stepfather, Peter, for his invaluable support.

Finally, I thank Kathrin for the special role she played in this work, and still does in my life.

Recipes

Vertical field Stark shift sample

1. Cleaning the sample
    - HCl dip with 1:1 HCl:H_2O for 60 s
    - Acetone/Isopropanol ultrasonic cleaning
2. Structuring the mesa
    - Spin coat sample with Az5214 1:0 at 4000 rpm for 35 s
    - Pre-bake at 100 °C for 60 s
    - Structure exposure using 3/4” mask with 25 s in soft contact mode
    - Develop in MIF726 for 30 s
    - Etch mesa
        - Mix 5g ferric nitrate, 4g Ethylene glycol and 2.5g H_2O
        - Remove 250 nm by etching for 180 s
3. Structuring the bottom contact
    - Spin coat sample with Az5214 1:0 at 4000 rpm for 35 s
    - Prebake at 100 °C for 60 s
    - Structure exposure using 5 mm mask for 25 s in soft contact mode
    - Develop in MIF726 for 30 s
    - Glue to glass sample holder with Az5214 1:0 and dry for 15 min at 100 °C

- Evaporate first to last:

material	layer thickness	deposition rates
Ge	15nm	0.4 Å/s
Au	30nm	0.5 Å/s
Ni	14nm	0.5 Å/s
Au	200nm	1.5 Å/s

- Acetone lift-off
- RTA at 440 °C for 120 s
- Remove organic residue for 10 min in O_2 plasma

4. Structuring the top contact – layer 1, Ti

   - Spin coat sample with Az5214 1:0 at 4000 rpm for 35 s
   - Pre-bake at 100 °C for 70 s
   - Structure exposure using the 3 mm mask for 5 s in soft contact mode
   - Structure exposure using the 170x170 μm mask mask for 5 s in soft contact mode (mask surface defects)
   - Reversal bake at 120 °C for 60 s
   - Flood exposure for 12 s
   - Develop in MIF726 for 30 s
   - Glue to glass sample holder with Az5214 1:0 and dry for 15 min at 100 °C
   - Evaporate 5 nm Ti
   - Acetone lift-off

5. Structuring the top contact – layer 1, Au shadow mask

   - Spin coat sample with Az5214 1:0 at 4000 rpm for 35 s
   - Pre-bake at 100 °C for 70 s
   - Rim exposure using 5 mm mask for 25 s in soft contact mode
   - Develop in Az351 1:4 for 45 s
   - Structure exposure 1 using 3 mm mask for 3 s in LVAC mode

- Structure exposure 2 using shadow mask (apertures) for 3 s in LVAC mode
- Structure exposure 3 using the 170x170 μm hole mask for 3 s in LVAC mode (mask surface defects)
- Reversal bake at 120 °C for 60 s
- Flood exposure for 15 s
- Develop in Az351 1:4 for 30 s
- Glue to glass sample holder with Az5214 1:0 and dry for 15 min at 100 °C
- Evaporate 100nm Au
- Acetone lift-off and delicate ultrasonic cleaning (20% 1min)

Bibliography

B. Alén, F. Bickel, K. Karrai, R.J. Warburton, and P.M. Petroff. Stark-shift modulation absorption spectroscopy of single quantum dots. *Applied Physics Letters*, 83:2235, 2003.

G. Bastard, E. E. Mendez, L. L. Chang, and L. Esaki. Variational calculations on a quantum well in an electric field. *Phys. Rev. B*, 28(6):3241–3245, Sep 1983.

D. Bimberg, M. Grundmann, and N.N. Ledentsov. *Quantum dot heterostructures*. Wiley, 1999.

Eliana Biolatti, Rita C. Iotti, Paolo Zanardi, and Fausto Rossi. Quantum information processing with semiconductor macroatoms. *Phys. Rev. Lett.*, 85(26):5647–5650, Dec 2000.

J. X. Chen, U. Oesterle, A. Fiore, R. P. Stanley, M. Ilegems, and T. Todaro. Matrix effects on the structural and optical properties of inas quantum dots. *Applied Physics Letters*, 79(22):3681–3683, 2001.

B. Damilano, N. Grandjean, F. Semond, J. Massies, and M. Leroux. From visible to white light emission by gan quantum dots on si(111) substrate. *Applied Physics Letters*, 75 (7):962–964, 1999.

D. J. Eaglesham and M. Cerullo. Dislocation-free stranski-krastanow growth of ge on si(100). *Phys. Rev. Lett.*, 64(16):1943–1946, Apr 1990.

R.J. Ellingson, M.C. Beard, J.C. Johnson, P. Yu, O.I. Micic, A.J. Nozik, A. Shabaev, A.L. Efros, et al. Highly efficient multiple exciton generation in colloidal PbSe and PbS quantum dots. *Nano Lett*, 5(5):865–871, 2005.

O. Engström, M. Kaniewska, Y. Fu, J. Piscator, and M. Malmkvist. Electron capture cross sections of inas/gaas quantum dots. *Applied Physics Letters*, 85(14):2908–2910, 2004.

Gernot Fasching. *Microcavity terahertz quantum-cascade lasers and single quantum dot microdevices.* PhD thesis, TU Vienna, 2006.

R. Ferreira and G. Bastard. Phonon-assisted capture and intradot auger relaxation in quantum dots. *Applied Physics Letters*, 74(19):2818–2820, 1999.

A. Fiore, P. Borri, W. Langbein, J. M. Hvam, U. Oesterle, R. Houdré, R. P. Stanley, and M. Ilegems. Time-resolved optical characterization of inas/ingaas quantum dots emitting at 1.3 mu m. *Applied Physics Letters*, 76(23):3430–3432, 2000.

P. W. Fry, I. E. Itskevich, D. J. Mowbray, M. S. Skolnick, J. J. Finley, J. A. Barker, E. P. O'Reilly, L. R. Wilson, I. A. Larkin, P. A. Maksym, M. Hopkinson, M. Al-Khafaji, J. P. R. David, A. G. Cullis, G. Hill, and J. C. Clark. Inverted electron-hole alignment in inas-gaas self-assembled quantum dots. *Phys. Rev. Lett.*, 84(4):733–736, Jan 2000.

J. M. Garcia, G. Medeiros-Ribeiro, K. Schmidt, T. Ngo, J. L. Feng, A. Lorke, J. Kotthaus, and P. M. Petroff. Intermixing and shape changes during the formation of inas self-assembled quantum dots. *Applied Physics Letters*, 71(14):2014–2016, 1997.

T. Grange, R. Ferreira, and G. Bastard. Polaron relaxation in self-assembled quantum dots: Breakdown of the semiclassical model. *Physical Review B (Condensed Matter and Materials Physics)*, 76(24):241304, 2007.

T. Grange, R. Ferreira, and G. Bastard. Theory of relaxation and decoherence of intersublevel transitions in semiconductor quantum dots. 193:012129, 2009.

SD Gunapala, SV Bandara, CJ Hill, DZ Ting, JK Liu, SB Rafol, ER Blazejewski, JM Mumolo, SA Keo, S. Krishna, et al. Demonstration of 640× 512 pixels long-wavelength infrared (LWIR) quantum dot infrared photodetector (QDIP) imaging focal plane array. *Infrared Physics and Technology*, 50(2-3):149–155, 2007.

Pawel Hawrylak. Excitonic artificial atoms: Engineering optical properties of quantum dots. *Phys. Rev. B*, 60(8):5597–5608, Aug 1999.

SY Hu, DB Young, SW Corzine, AC Gossard, and LA Coldren. High-efficiency and low-threshold InGaAs/AlGaAs quantum-well lasers. *Journal of Applied Physics*, 76:3932, 1994.

C.Y. Huang, T.M. Ou, S.T. Chou, C.S. Tsai, M.C. Wu, S.Y. Lin, and J.Y. Chi. Temperature dependence of carrier dynamics for InAs/ GaAs quantum dot infrared photodetectors. *Journal of Vacuum Science & Technology B: Microelectronics and Nanometer Structures*, 23:1909, 2005.

D. L. Huffaker and D. G. Deppe. Electroluminescence efficiency of 1.3 mu m wavelength ingaas/gaas quantum dots. *Applied Physics Letters*, 73(4):520–522, 1998.

T. Inoshita and H. Sakaki. Electron relaxation in a quantum dot: Significance of multiphonon processes. *Phys. Rev. B*, 46(11):7260–7263, Sep 1992.

S. Kaiser, T. Mensing, L. Worschech, F. Klopf, J. P. Reithmaier, and A. Forchel. Optical spectroscopy of single inas/ingaas quantum dots in a quantum well. *Applied Physics Letters*, 81(26):4898–4900, 2002.

Shigeru Kohmoto, Hitoshi Nakamura, Tomonori Ishikawa, and Kiyoshi Asakawa. Site-controlled self-organization of individual inas quantum dots by scanning tunneling probe-assisted nanolithography. *Applied Physics Letters*, 75(22):3488–3490, 1999.

G.T.A. Kovacs. *Micromachined transducers sourcebook.* Boston, 1998.

Michael Krall. Optical spectroscopy and electrical control of self-assembled quantum dots. Master's thesis, TU Vienna, 2008.

H. Kressel, J. U. Dunse, H. Nelson, and F. Z. Hawrylo. Luminescence in silicon-doped gaas grown by liquid-phase epitaxy. *Journal of Applied Physics*, 39(4):2006–2011, 1968.

L. Landin, MS Miller, M.E. Pistol, CE Pryor, and L. Samuelson. Optical studies of individual InAs quantum dots in GaAs: few-particle effects. *Science*, 280(5361):262, 1998.

E. C. Le Ru, P. Howe, T. S. Jones, and R. Murray. Strain-engineered inas/gaas quantum dots for long-wavelength emission. *Phys. Rev. B*, 67(16):165303, Apr 2003.

D. Leonard, K. Pond, and P. M. Petroff. Critical layer thickness for self-assembled inas islands on gaas. *Phys. Rev. B*, 50(16):11687–11692, Oct 1994.

X. Li, Y. Wu, D. Steel, D. Gammon, TH Stievater, DS Katzer, D. Park, C. Piermarocchi, and LJ Sham. An all-optical quantum gate in a semiconductor quantum dot. *Science*, 301(5634):809, 2003.

G.T. Liu, A. Stintz, H. Li, L.F. Lester, and K.J. Malloy. Ultralow-threshold-current-density quantum dot lasers using the dots-in-a-well (DWELL) structure. In *Proceedings of SPIE*, volume 3944, page 814, 2000.

D. Loss and D.P. DiVincenzo. Quantum computation with quantum dots. *Physical Review A*, 57(1):120–126, 1998.

I.V. Markov. *Crystal growth for beginners*. World scientific Singapore, 1995.

Y. Masumoto and T. Takagahara. *Semiconductor Quantum Dots*. Springer, 2002.

Z. Mi, P. Bhattacharya, and S. Fathpour. High-speed 1.3 μm tunnel injection quantum-dot lasers. *Applied Physics Letters*, 86:153109, 2005.

D. A. B. Miller, D. S. Chemla, T. C. Damen, A. C. Gossard, W. Wiegmann, T. H. Wood, and C. A. Burrus. Band-edge electroabsorption in quantum well structures: The quantum-confined stark effect. *Phys. Rev. Lett.*, 53(22):2173–2176, Nov 1984.

D. A. B. Miller, D. S. Chemla, T. C. Damen, A. C. Gossard, W. Wiegmann, T. H. Wood, and C. A. Burrus. Electric field dependence of optical absorption near the band gap of quantum-well structures. *Phys. Rev. B*, 32(2):1043–1060, Jul 1985.

T. Müller, F. F. Schrey, G. Strasser, and K. Unterrainer. Ultrafast intraband spectroscopy of electron capture and relaxation in inas/gaas quantum dots. *Applied Physics Letters*, 83(17):3572–3574, 2003.

TC Newell, DJ Bossert, A. Stintz, B. Fuchs, KJ Malloy, and LF Lester. Gain and linewidth enhancement factor in InAs quantum-dot laser diodes. *IEEE Photonics Technology Letters*, 11(12):1527–1529, 1999.

L. Pavesi, L.D. Negro, C. Mazzoleni, G. Franzo, and F. Priolo. Optical gain in silicon nanocrystals. *Nature*, 408(6811):440–444, 2000.

JR Petta, AC Johnson, JM Taylor, EA Laird, A. Yacoby, MD Lukin, CM Marcus, MP Hanson, and AC Gossard. Coherent manipulation of coupled electron spins in semiconductor quantum dots. *Science*, 309(5744):2180, 2005.

P. Photopoulos and AG Nassiopoulou. Room-and low-temperature voltage tunable electroluminescence from a single layer of silicon quantum dots in between two thin SiO layers. *Applied Physics Letters*, 77:1816, 2000.

H. J. Polland, L. Schultheis, J. Kuhl, E. O. Göbel, and C. W. Tu. Lifetime enhancement of two-dimensional excitons by the quantum-confined stark effect. *Phys. Rev. Lett.*, 55 (23):2610–2613, Dec 1985.

G.A. Reider. *Photonik*. Springer, 2004.

I. Robel, V. Subramanian, M. Kuno, P.V. Kamat, et al. Quantum dot solar cells. Harvesting light energy with CdSe nanocrystals molecularly linked to mesoscopic TiO2 films. *Journal of the American Chemical Society*, 128(7):2385–2393, 2006.

Hideaki Saito, Kenichi Nishi, and Shigeo Sugou. Influence of gaas capping on the optical properties of ingaas/gaas surface quantum dots with 1.5 mu m emission. *Applied Physics Letters*, 73(19):2742–2744, 1998.

A. Salhi, Y. Rouillard, A. Perona, P. Grech, M. Garcia, and C. Sirtori. Low-threshold GaInAsSb/AlGaAsSb quantum well laser diodes emitting near 2.3 μm. *Semiconductor Science and Technology*, 19:260–262, 2004.

S. Sauvage, P. Boucaud, T. Brunhes, A. Lemaître, and J.-M. Gérard. Midinfrared unipolar photoluminescence in inas/gaas self-assembled quantum dots. *Phys. Rev. B*, 60(23): 15589–15592, Dec 1999.

S. Sauvage, P. Boucaud, F. H. Julien, J.-M. Gérard, and J.-Y. Marzin. Infrared spectroscopy of intraband transitions in self-organized inas/gaas quantum dots. *Journal of Applied Physics*, 82(7):3396–3401, 1997a.

S. Sauvage, P. Boucaud, FH Julien, J.M. Gerard, and V. Thierry-Mieg. Intraband absorption in n-doped InAs/GaAs quantum dots. *Applied Physics Letters*, 71:2785, 1997b.

R. D. Schaller and V. I. Klimov. High efficiency carrier multiplication in pbse nanocrystals: Implications for solar energy conversion. *Phys. Rev. Lett.*, 92(18):186601, May 2004.

W. Seifert, N. Carlsson, P. Castrillo, D. Hessman, J. Johansson, ME Pistol, and L. Samuelson. Quantum Dots Grown In-Situ by MOVPE: Sizes, Densities and Optical Properties. *BRAZILIAN JOURNAL OF PHYSICS*, 27:3–11, 1997.

T. Shimbori and T. Kobayashi. Stationary flows of the parabolic potential barrier in two dimensions. *Journal of Physics A: Mathematical and General*, 33:7637–7652, 2000.

A.D. Stiff, S. Krishna, P. Bhattacharya, and S.W. Kennerly. Normal-incidence, high-temperature, mid-infrared, InAs-GaAs vertical quantum-dot infrared photodetector. *IEEE Journal of Quantum Electronics*, 37(11):1412–1419, 2001.

D. Strauch and B. Dorner. Phonon dispersion in GaAs. *Journal of Physics: Condensed Matter*, 2:1457–1474, 1990.

S.F. Tang, C. Chiang, P. Weng, Y. Gau, J. Luo, S. Yang, C. Shih, S. Lin, and S. Lee. High-temperature operation normal incident 256× 256 InAs-GaAs quantum-dot infrared photodetector focal plane array. *IEEE Photon. Technol. Lett*, 18:986–988, 2006.

A. Wallrabe. *Nachtsichttechnik*. Vieweg, 2001.

U. Woggon. *Optical properties of semiconductor quantum dots*. Springer-Verlag Berlin, 1996.

P. Yu, M.C. Beard, R.J. Ellingson, S. Ferrere, C. Curtis, J. Drexler, F. Luiszer, and A.J. Nozik. Absorption cross-section and related optical properties of colloidal InAs quantum dots. *J. Phys. Chem. B*, 109(15):7084–7087, 2005.